THESIS

FUTURE PROJECTIONS OF THE 2011 SUPER TORNADO OUTBREAK UNDER GLOBAL WARMING AND STRATOSPHERIC AEROSOL INJECTION

Submitted by

Bali Summers

Department of Atmospheric Science

In partial fulfillment of the requirements

For the Degree of Master of Science

Colorado State University

Fort Collins, Colorado

Summer 2025

Master's Committee:

Advisor: James W. Hurrell
Co-Advisor: Kristen L. Rasmussen

Frances V. Davenport

ABSTRACT

FUTURE PROJECTIONS OF THE 2011 SUPER TORNADO OUTBREAK UNDER GLOBAL WARMING AND STRATOSPHERIC AEROSOL INJECTION

Disasters associated with hazardous convective weather including severe thunderstorms, tornadoes, strong winds, large hail, and flooding, have been increasing in both frequency and cost. Previous studies using convection-permitting regional models show that climate change is likely to produce a future with fewer weak thunderstorms but more strong storms through increases in both convective available potential energy and convective inhibition. To potentially mitigate some of the threatening impacts of global warming, climate intervention strategies aiming to offset anthropogenic surface warming are receiving increased attention. One proposed approach is stratospheric aerosol injection (SAI), in which reflective aerosol particles would be injected into the upper atmosphere to decrease a small percentage of the total incoming solar radiation, thereby reducing future rates of warming. Little to no research has been conducted on the impacts from this possible strategy on severe weather using a convection-permitting model. We conduct novel simulations of the 2011 Super Tornado Outbreak using a 4-km version of the Weather and Research Forecasting (WRF) model to examine how this severe weather outbreak might be different in the future under two greenhouse gas emission scenarios with and without SAI. We find broadly that numerous parameters closely related to storm severity increase in a future with climate change, while parameter changes are minimal under climate change with SAI. To the best of our knowledge, this is the first study to consider the effects of SAI on mesoscale processes using a model like WRF.

TABLE OF CONTENTS

CHAPTER 1

INTRODUCTION

Hazards associated with extreme weather including severe thunderstorms, tornadoes, strong winds, large hail, and flooding, have been increasing in both frequency and cost since the 1980s (NCEI, 2025). The year 2023, for instance, was record breaking with weather and climate related disasters accounting for ~$28B in damages, with roughly two-thirds of that amount coming from severe weather (NCEI, 2025). Since severe weather events cause significant loss of life and property in the U.S. and globally (World Economic Forum, 2025), there is concern regarding how dangerous these events may be in the future under the effects of climate change. Previous studies examining future changes in severe thunderstorm days agree that environments favorable for severe thunderstorm production will occur more frequently in a warmer climate (H. E. Brooks, 2013; Diffenbaugh et al., 2013; Seeley & Romps, 2015; Trapp et al., 2007).

To potentially mitigate some of the most threatening impacts of global warming, climate intervention strategies aiming to offset anthropogenic surface warming are receiving increased attention. One proposed approach is stratospheric aerosol injection (SAI), in which sulfur dioxide (a precursor to highly reflective sulfate aerosols) would be injected into the upper atmosphere to reflect a small percentage of the total incoming solar radiation, thereby reducing future rates of warming. While greenhouse gases act to warm the Earth's surface by absorbing outgoing longwave radiation and reemitting a portion of it back toward the surface, stratospheric aerosols reflect incoming shortwave radiation away from the Earth, resulting in surface cooling. SAI is one of the best studied climate intervention approaches (NASEM, 2021), in part because some volcanic eruptions serve as a natural analogue (Minnis et al., 1993; Robock, 2000). Observed periods of

global cooling following large volcanic eruptions have been well documented and attributed to the lofting of sulfurous aerosol compounds into the stratosphere (Minnis et al., 1993; Robock, 2000; Schmidt et al., 2018; Timmreck, 2012). While SAI would not address greenhouse gas emissions, which are the root cause of climate change, SAI may be a feasible method of reducing climate risk (The Royal Society, 2009), thus serving as a complement to emissions reduction and greenhouse gas removal efforts (Buck, 2022; Long & Shepherd, 2014). Furthermore, SAI is estimated to be more cost effective than many other potential climate interventions (Smith, 2020), and it has one of the highest potentials for radiational cooling (Lenton & Vaughan, 2009).

Previous studies have used Earth system models to examine the potential impacts of SAI on temperature and precipitation (Hueholt et al., 2023; Richter et al., 2022; Tilmes et al., 2018), atmospheric circulation (Bednarz et al., 2022), extreme temperature and precipitation events (Barnes et al., 2022; Ji et al., 2018), wildfire risk (Touma et al., 2023), ecological responses (Hueholt et al., 2024; Zarnetske et al., 2021), Arctic sea ice (Lee et al., 2023; Morrison et al., 2024), large-scale environments supporting convective weather (Glade et al., 2023), and extratropical cyclones (Reboita et al., 2024). However, little to no research has been conducted on the possible impacts of SAI on severe weather using a convection-permitting (also known as km-scale) model that allows for a more realistic representation of mesoscale weather events, including organized convection and the diurnal cycle of precipitation (Rasmussen et al., 2017). To comprehensively assess the potential benefits and risks of SAI relative to the risks posed by climate change, it is important to understand how convective weather might change in the future with and without SAI.

Coarse resolution climate models are commonly used to simulate future climates and to examine the impact of different rates of greenhouse gas emissions or climate interventions (O'Neill

et al., 2016; Richter et al., 2022; Tilmes et al., 2018). These models are often used to simulate long periods of time, which is necessary in order to distinguish forced climatological changes (as with anthropogenic emissions) from internal climate variability. However, due to their coarse resolution, climate models have challenges representing organized convective systems (Ban et al., 2015), the diurnal cycle of precipitation (Allen & Ingram, 2002; Dai, 2006; Dai & Trenberth, 2004), and sub-grid cloud processes. On the other hand, directly simulating long-term changes to the global climate with a convection-permitting model is computationally expensive. Previous studies investigating hazardous convective weather events in a future climate (Carroll-Smith et al., 2021; E. M. Dougherty et al., 2023; E. Dougherty & Rasmussen, 2020; Trapp & Hoogewind, 2016) typically use a method of downscaling referred to as the "pseudo-global warming" method or PGW method. In short, the PGW method applies a perturbation (e.g. a temperature change) to the historical climate information used in the model input in order to simulate a future climate (Ekström et al., 2015; Liu et al., 2017). Studies using the PGW method note the ability of this technique to accurately represent observed storm structure and timing of convective weather events (E. M. Dougherty et al., 2023; E. Dougherty & Rasmussen, 2020). An important caveat of the PGW method, however, is its inability to allow the synoptic scale forcing to evolve freely, meaning that potential changes in the location of the jet stream or storm tracks and the downstream effects of these changes cannot be assessed with this method (Liu et al., 2017). The PGW method will be described in further detail in the methods section of the paper.

In this study, we conducted novel simulations of the 2011 Super Tornado Outbreak using the Weather and Research Forecasting model at 4-km horizontal grid spacing to examine how this record-breaking severe weather outbreak might look in the future under different greenhouse gas emission and SAI scenarios. The 2011 Super Tornado Outbreak was a four-day event from April

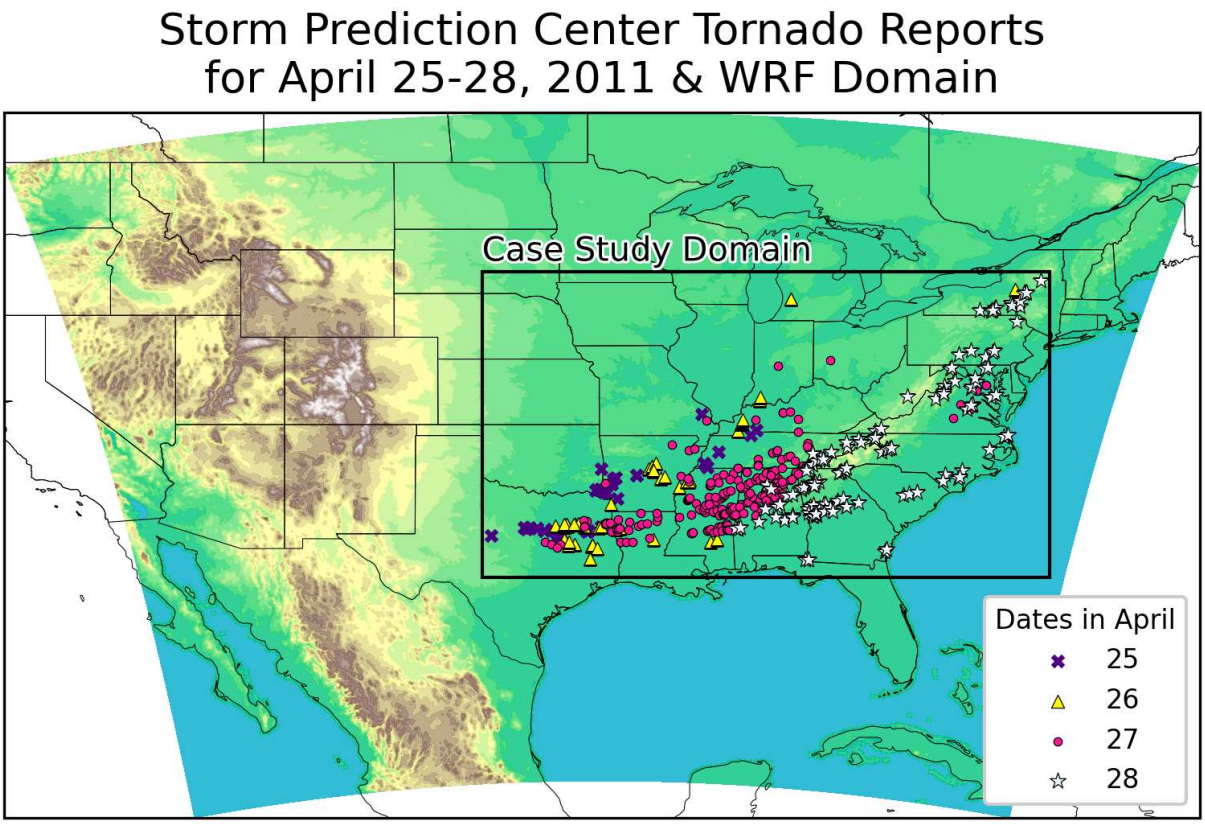

Figure 1.1: Storm prediction center tornado reports are labeled by the day they occurred in the tornado outbreak according to UTC time. Colored contours show terrain features and the extent of the WRF model domain. The black rectangle outlines the region analyzed in this study, representing the area of most active convection and tornadic activity lying within the larger WRF domain.

25th to 28th. It produced approximately 356 tornados, of which April 27th was the most active day with a record-breaking 199 tornadoes in 24 hours (Knupp et al., 2014). Figure 1.1 shows the locations of tornado reports from the Storm Prediction Center archive. There were also an estimated 321 deaths and $12B in losses during the four-day outbreak, making it one of the deadliest and most expensive weather disasters in history (NOAA, 2021). This tornado outbreak event was associated with an extratropical cyclone that moved slowly over the eastern United States and produced quasi-linear convective systems, mesoscale convective vortices, supercells, and tornadoes in the warm sector (Chasteen & Koch, 2022; Knupp et al., 2014). The storm system was synoptically forced by an upper-level trough, as shown in Figure 1.2 (Chasteen & Koch,

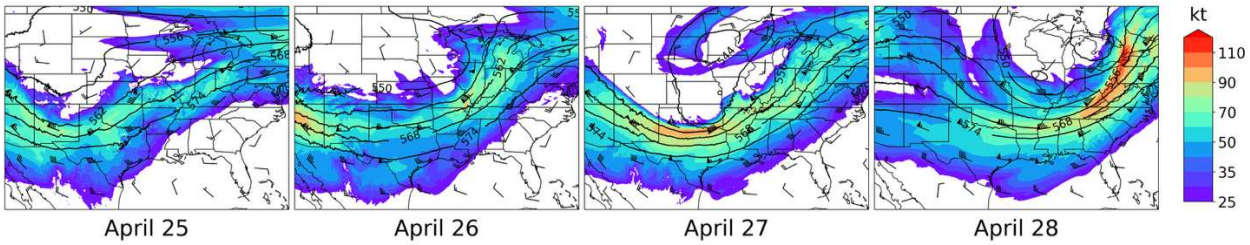

Figure 1.2: 500 mb heights (dm) and winds (barbs and contours, kt) from the CTRL simulation at 00 UTC on each day of the 2011 Super Tornado Outbreak.

2022). A strong jet streak moved from behind to in front of the trough, which is a clear indication of a strengthening baroclinic system and a pattern known to support supercell and tornadic activity in the Southeast (Chasteen & Koch, 2022; Guyer, 2006). The meteorological details of the 2011 Super Tornado Outbreak have been thoroughly examined in prior research (Chasteen & Koch, 2022; Knupp et al., 2014), making it a good candidate to assess how a hazardous convective weather event might change in different future climates.

An ingredients-based analysis is a common practice for forecasting hazardous weather environments, including severe convection, supercell thunderstorms, tornadic environments, as well as hail and other hazards less pertinent to this case study (Harold E. Brooks, 2007). Studies examining this event cited significant convective available potential energy (CAPE), intense updrafts, strong vertical wind shear, and large storm relative helicity (SRH) as some of the contributing factors to its anomalously intense nature (Chasteen & Koch, 2022; Knupp et al., 2014). Additionally, an ingredients-based perspective has been used in a case study of flash-flood producing storms in convection-permitting simulations of future climates (Dougherty & Rasmussen, 2020). By assessing the changes in environmental parameters supporting this hazardous convective weather event as a proxy for the potential occurrence or intensity of severe weather, we are able to consider how this event could change under a different future climate. In

the work presented here we will examine how the 2011 Super Tornado Outbreak might be changed by changes to the large-scale environments by the mid-21st century with and without SAI.

CHAPTER 2

METHODOLOGY AND EXPERIMENTAL DESIGN

2.1 Simulations

High-resolution convection-permitting regional climate simulations were conducted with the Weather and Research Forecasting (WRF) model V4.1.5 (Skamarock et al., 2008). They cover most of the contiguous United States (CONUS) with a domain of 1360 x 1016 grid points at 4-km horizontal grid spacing with 61 vertically-stretched levels capped at 10 hPa. The model domain is shown in Figure 1.1. Parameterizations used in our simulations include the Thompson microphysics scheme (Thompson et al., 2008), the Yonsei University planetary boundary layer scheme (Hong et al., 2006), the Noah-MP land surface model (Niu et al., 2011), and the Rapid Radiative Transfer Model (RRTMG) for longwave and shortwave atmospheric radiation (Iacono et al., 2008). For more details, see Sun et al. (2025).

A control simulation (CTRL) was conducted to represent the observed weather over the months of March to August 2011, using ERA5 reanalysis data (Hersbach et al., 2020) to force the lateral and lower boundaries every hour. To simulate future climate states, a pseudo-global warming (PGW) approach was applied, as in previous studies (Dai et al., 2020; E. Dougherty & Rasmussen, 2020; Gutmann et al., 2018; Liu et al., 2017; K. L. Rasmussen et al., 2017; R. Rasmussen et al., 2011, 2014; Schär et al., 1996).

As described in Sun et al. (2025), a climate delta was added to the ERA5 input, as follows:

$$\mathrm{WRF}_{\mathrm{PGW\,INPUT}} = \mathrm{ERA5} + \Delta\mathrm{CESM} \quad (1)$$

where ΔCESM is the climate delta signal obtained from the Community Earth System Model (CESM) (Danabasoglu et al., 2020) under different climate change scenarios between two 10-year periods:

$$\Delta\mathrm{CESM} = \mathrm{CESM}_{2060-2069} - \mathrm{CESM}_{2015-2024} \quad (2)$$

Specifically, the climate delta is added to the ERA5 data in the horizontal wind, geopotential, temperature, and specific humidity along the regional boundaries, and along the lower boundary it is added to the sea surface temperature, soil temperature, sea level pressure, and sea ice.

To examine future climate states under SAI, we used information from the Assessing Responses and Impacts of Solar climate Intervention on the Earth system with stratospheric aerosol injection (ARISE) experiment (Richter et al., 2022) and the Stratospheric Aerosol Geoengineering Large Ensemble (GLENS) project (Tilmes et al., 2018). These experiments use the moderate Shared Socioeconomic Pathway scenario (SSP2-4.5) (O'Neill et al., 2016) and high emission scenario Representative Concentration Pathway 8.5 (RCP8.5) (van Vuuren et al., 2011), respectively. These emissions scenarios are used to examine future climate states under global warming without SAI for comparison. The SSP2-4.5 and ARISE experiments were run with the Community Earth System Model 2 with the Whole Atmosphere Community Climate Model (CESM2-WACCM) (Richter et al., 2022), whereas the RCP8.5 and GLENS simulations were run with the Community Earth System Model 1 with the Whole Atmosphere Community Climate Model (CESM1-WACCM) (Tilmes et al., 2018).

Notably, the implementation of SAI in ARISE and GLENS have different goals and different start dates. SAI deployment in GLENS begins in 2020 and aims to maintain climate conditions representative of 2020, including the global mean surface temperature, the north-south interhemispheric temperature gradient, and the equator-to-pole temperature gradient (Tilmes et al., 2018). SAI deployment in ARISE begins in 2035 and aims to maintain the same climate variables

as in GLENS, but with respect to the 2020-2039 time period, which corresponds to when the simulated global mean temperature is near 1.5˚C above preindustrial levels (Richter et al., 2022).

By using a high end emissions scenario (Hausfather & Peters, 2020) requiring large injections of SO2 to offset the resultant warming in GLENS, the signal-to-noise ratio of the climate change and SAI simulations are maximized (Tilmes et al., 2018). SSP2-4.5, on the other hand, more closely represents current emission rates and policy (Burgess et al., 2020). Richter et al. (2022) state, "The ARISE-SAI simulations are designed to simulate a plausible implementation scenario of [solar climate intervention] using SAI for evaluation of potential climate intervention risks and impacts." These differences provide important context in considering the effects observed in the simulations examined here. Since SSP2-4.5 and ARISE represent "plausible" warming and SAI scenarios, the response to the warming or SAI will likely be more muted than in the RCP8.5 and GLENS simulations. The RCP8.5 and GLENS simulations represent less "plausible" futures, but they provide context to the possible range of risk and likely produce more clear responses to the climatic changes.

Climatic information extracted from the ARISE and GLENS experiments is the same as the information in the climate deltas from the SSP2-4.5 and RCP8.5 scenarios, with the addition of the average monthly difference in the aerosol optical depth (AOD) between 2015-2024 and 2060-2069 (Sun et al. 2025). We refer to this method of simulating SAI in a future climate as a pseudo stratospheric aerosol injection (PSAI) method. Climate deltas from the ARISE and GLENS experiments were added to the ERA5 input to produce PSAI simulations, as follows:

$$\mathrm{WRF}_{\mathrm{PSAI\ INPUT}} = \mathrm{ERA5} + \Delta\mathrm{CESM}_{\mathrm{ARISE/GLENS}} \quad (3)$$

The AOD delta from the ARISE and GLENS experiments was input into the RRTMG shortwave radiation scheme and is a novel contribution to the representation of SAI in mesoscale

modeling. It is important to note that our study does not represent aerosol effects explicitly, as the aerosols that contribute to large increases in AOD in the stratosphere do not interact directly with clouds and precipitation (Sun et al. 2025). Thus, this approach represents the reduction in incoming shortwave solar radiation as a result of increased AOD in the stratosphere.

Additionally, climate deltas were calculated from the ensemble-mean of the CESM experiments. Decadal changes in the climate from a singular climate model run may contain large internal variability due to the effects of natural regional climate variations, and thus are sometimes not representative of the forced response from anthropogenic climate change (Deser et al., 2012). Thus, the climate deltas are calculated from an ensemble of climate model runs in order to reduce the influence of internal climate variability on the decadal changes (Liu et al., 2017; Trapp et al., 2021). Specifically, the ARISE simulations had 10 ensemble members and the GLENS simulations had 21 ensemble members. The simulations of SSP2-4.5 had 5 ensemble members for both the 2015-2024 period and the 2060-2069 period (Richter et al., 2022), whereas the simulations of RCP8.5 had 17 ensemble members for the 2015-2024 period and 4 ensemble members for the 2060-2069 period (Tilmes et al., 2018).

Although the model output spans from March to August of 2011 and covers the CONUS, we limit our analysis for this study to the region and period pertinent to the Super Tornado Outbreak of 2011 (Figure 1.1). Specifically, we analyze April 25th to 28th of 2011, hereafter referred to as the event period, and we examine the area within -100˚ to -74˚longitude and 30˚ to 44˚ latitude, hereafter referred to as the event region. This region was chosen because it captures all of the tornadoes that occurred during the outbreak as well as the majority of the intense convective character of the storm system, as defined by the Tropical Rainfall Measuring Mission (TRMM) heritage storm modes (described later).

2.2 Atmospheric Moisture and Precipitation Analysis

Atmospheric moisture is a key ingredient for deep convection and intense precipitation (Johns & Doswell, 1992), and rainfall rates are necessary for documenting precipitation intensity. We examine precipitable water (mm), accumulated precipitation (mm), and precipitation rates (mm hr-1), which are part of the direct hourly outputs from WRF, to understand how these variables could change in different climate futures. To assess the general robustness of the WRF simulation of the 2011 Super Tornado Outbreak, daily accumulated precipitation from the CTRL simulation is compared to NCEP/EMC 4 km gridded Stage IV data (Du, 2011). The Stage IV dataset is a rain gauge corrected radar observational dataset, and the daily precipitation totals are acquired by taking a sum of the hourly accumulated precipitation from each hour in a day.

2.3 Thermodynamic Environments

We also examine how the thermodynamic environments supporting the 2011 Super Tornado Outbreak might change in future climates. Thermodynamic variables including convective available potential energy (CAPE; J kg^{-1}) and convective inhibition (CIN; J kg^{-1}) are calculated with hourly output from the WRF simulations. CAPE is a measure of the buoyant energy from the level of free convection to the equilibrium level and is often used to assess the potential for severe convective weather. CIN is the negative buoyant energy from the parcel's starting point to its level of free convection. The amount of CIN present in the environment determines whether it will be conducive or unconducive for convective weather. Specifically, the maximum CAPE and maximum CIN are calculated by first computing the maximum theta-e height level in the lowest

3000 m, centering a 500 m deep parcel over the maximum theta-e height, then computing the maximum CAPE and CIN from this parcel's average moisture and temperature characteristics (Doswell & Rasmussen, 1994). Previous studies using convection-permitting regional models have found that climate change is likely to produce a future with fewer weak thunderstorms but more strong storms over the U.S. (Liu et al., 2024; K. L. Rasmussen et al., 2017). This is due to increases in both CAPE and CIN in a warmer climate, marking the importance of examining both parameters (Hoogewind et al., 2017; Liu et al., 2024; K. L. Rasmussen et al., 2017; Trapp et al., 2019).

2.4 Mesoscale Analysis

To assess the impact of global warming and SAI on the mesoscale characteristics of the 2011 Super Tornado outbreak, analyses focused on reflectivity, updraft velocity, and updraft helicity are conducted. Each is evaluated with respect to one or more cutoff thresholds, since the signal indicating changes in different future climates may be muted or unclear if entire populations are examined. Where possible we choose thresholds based on operationally-relevant values used for forecasting severe weather, although in some cases these thresholds had to be lowered so that enough points were included for the pattern of the signal to be clear.

One characteristic is the maximum updraft speed. Strong updrafts are a key ingredient of convection (Johns & Doswell, 1992); hence, updraft strength is directly related to the severity of the convective precipitating system. For instance, Deierling & Petersen (2008) found that large updraft volumes of high speed are connected with lightning activity by producing more mixed phase hydrometeors and therefore more collisions between them. We use maximum updraft speeds of 5 m s^{-1} and 15 m s^{-1} indicating mild and intense upward motion respectively.

Simulated three dimensional radar reflectivity (dBZ) is another useful indicator of storm intensity (Haberlie et al., 2022; K. L. Rasmussen et al., 2017). Reflectivity is a measure of power reflected off of particles in the air (generally hydrometeors), which depends on the number and size of particles present in an area. As in Rasmussen et al. (2017), 0 dBZ is the lowest reflectivity value considered, 0-20 dBZ represents weak convection, 20-40 dBZ represents moderate convection, and greater than 40 dBZ is considered to be strong convection. Storm height is often directly related to storm intensity as stronger storms often have faster updrafts and can support larger and more concentrated mixed-phase hydrometeors high in the atmosphere (Deierling & Petersen, 2008; Zipser et al., 2006). Given that this study focuses on a record-breaking severe tornado outbreak, reflectivity values occurring lower than 10 km in the atmosphere are not considered to focus on the reflectivity echoes highest in the storm. In the same vein, analysis of echo top height (km), or the height of the highest occurrence of a specific reflectivity value, is also performed.

Updraft helicity (UH), or the helical character of upward motion, has been used in research and in operational forecasting for identifying severe storm environments. In a study by Sobash et al. (2016), they noted the skill of UH > 120 m^2 s^{-2} occurring from 0-3 km (UH03) above ground level (AGL) in forecasting tornadic environments from km-scale WRF simulations with low false alarm rates. UH is calculated with the formula from (Kain et al., 2008), which is as follows:

$$\mathrm{UH} = \int_{z_0}^{z_1} w\zeta \, dz \tag{4}$$

where ζ is the vertical component of the relative vorticity.

Histograms of mesoscale indices of storm severity and the spatial frequency of these characteristics are assessed with the same methods as described previously. Additionally, the change in occurrence of thresholded mesoscale indices from the control simulation to the PGW

and PSAI simulations is considered to investigate how the occurrence of extreme storm characteristics may change. To do this, the number of pixels that breached the given threshold across spatial and temporal dimensions are counted. The count from the control simulation is then subtracted, and then the value is divided by the count from the control simulation. Finally, the fraction is multiplied by 100, as follows:

$$\% \Delta P_{PGW/PSAI} = \frac{\sum P_{PGW/PSAI} - \sum P_{CTRL}}{\sum P_{CTRL}} \times 100 \quad (5)$$

where P is a count of the pixels that exceed a given threshold. It is important to note that because we look at very high thresholds for the examined variables, these calculations can sometimes produce large changes in the percent occurrence when there are very few total occurrences.

2.5 Storm Modes

Another method of analyzing storm character is identifying types of precipitating cloud structures, or storm modes, based on the height, width, intensity, and stratiform versus convective character of the storm structures (Houze et al., 2015). This method was originally developed for spaceborne satellite radar studies (TRMM) (Houze et al., 2015) and has been used to characterize the occurrence of a variety of storm modes globally (Houze et al., 2019; Panasawatwong et al., 2022; K. L. Rasmussen & Houze, 2016). First, simulated reflectivity is separated into stratiform and convective precipitation regions. Stratiform and convective precipitation are defined by the mechanism through which the precipitation is formed. Stratiform precipitation is formed via vapor deposition due to small vertical velocities, whereas convective precipitation is due to strong vertical velocities causing precipitation to form through coalescence and riming (Houghton, 1968; Houze, 1994). Additionally, stratiform precipitation regions tend to be weaker, longer-lived, and more widespread, whereas convective precipitation tends to be intense and short-lived. In practice,

however, stratiform versus convective precipitation are separated using reflectivity (Houze Jr. et al., 2015; Steiner et al., 1995). As in Steiner et al. (1995), convection is identified by intensity, or 40 dBZ or higher reflectivity echoes, peakedness, and the surrounding area. Peakedness describes a sufficient difference in reflectivity compared to the background reflectivity. Identification from the surrounding area means any grid point within a certain radius surrounding a convective center identified by the other two methods is also considered to be convection. Stratiform precipitation is identified by any remaining areas of reflectivity of 15 dBZ or greater.

After this, precipitation systems are classified into different types, or storm modes, depending on their height in the atmosphere and their horizontal spatial extent. Storm modes include deep convective cores (DCCs; 40 dBZ reflectivity echo cores ≥ 10 km in altitude), wide convective cores (WCCs; 40 dBZ reflectivity echo cores ≥ 1,000 km^2 horizontally), deep and wide convective cores (DWCCs; reflectivity cores that are classified as both a DCC and WCC), and broad stratiform regions (BSRs; contiguous stratiform pixels ≥ 50,000 km^2). These storm categories were originally developed to evaluate the nature of convective storms on a global scale, including regions with the deepest and widest convective storms on Earth (Houze et al., 2015). In regions with frequent mesoscale convective systems (MCSs), storm modes often represent a storm lifecycle, wherein strong storms initiate and develop DCCs and then merge together with other systems as they organize on the mesoscale (Rasmussen & Houze, 2011). As the MCSs enter their mature and decaying phase, they often develop robust stratiform regions. By identifying specific storm modes within the case study examined in this work, a broader view into the three-dimensional characteristics of the storm are possible.

CHAPTER 3

RESULTS

In this study we examine the thermodynamics, precipitation, mesoscale indices of severe weather, and storm modes of the 2011 Super Tornado Outbreak under future climates with different rates of greenhouse gas emissions and different implementations of SAI. We aim to understand how these characteristics may change for this event under SAI in order to assess the potential benefits and risks involved with SAI in comparison to the risks posed by climate change.

3.1 Thermodynamics and Moisture

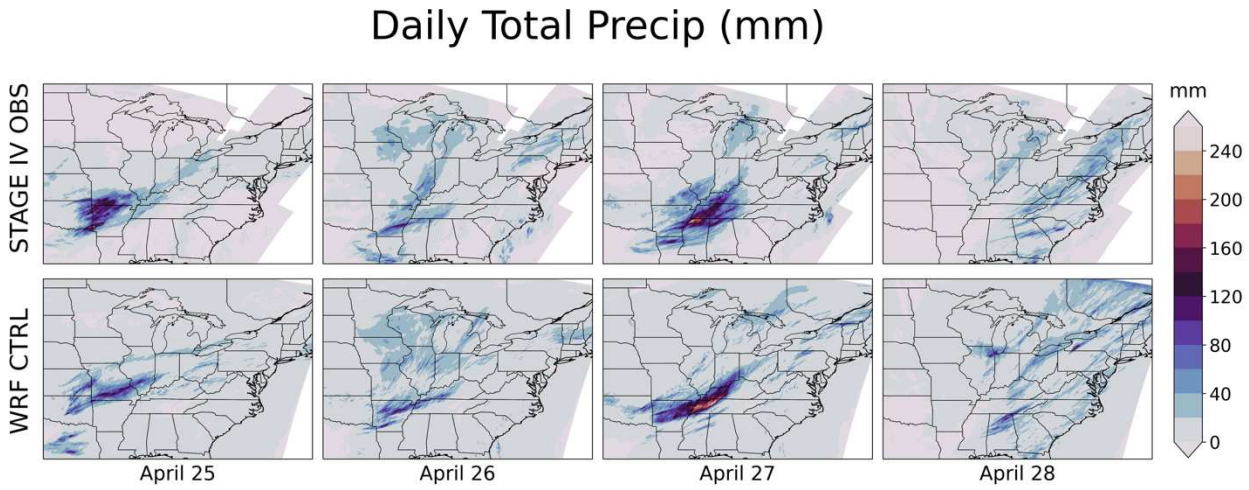

Figure 3.1: Daily accumulated precipitation (mm) from Stage IV Observations (top) and the WRF CTRL (bottom) simulation for the days of the 2011 Tornado Outbreak.

We begin by evaluating the precipitation patterns in the CTRL run compared to observations. The accumulated daily precipitation of the CTRL simulation compares well to the stage IV observational dataset (Figure 3.1) in terms of spatial extent, general structure, and magnitude of precipitation. The structure of the precipitation in the CTRL run matches especially well to the stage IV precipitation on April 26th through the 28th. April 26th, for instance, is

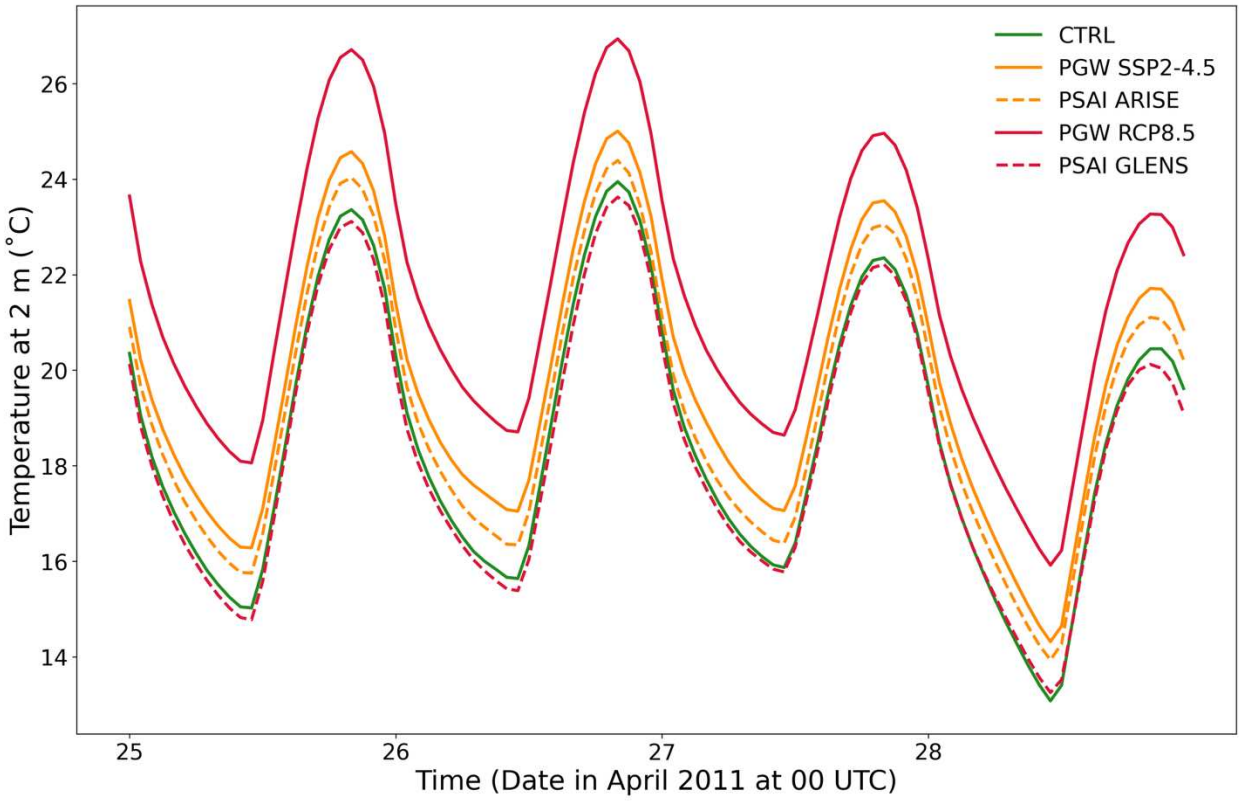

Figure 3.2: Mean temperature at 2 m (˚C) in the event region from 00 UTC April 25th to 23 UTC April 28th, 2011 for the CTRL, PGW, and PSAI simulations.

characterized by a line of precipitation from Arkansas to Kentucky in both CTRL and observations. The area of highest accumulated precipitation in the CTRL on the 27th is well geographically located and shows a similar curve as in the observations, though may perhaps be missing some of the broader rainfall of lesser intensity. On the 28th, there is agreement between the two on the scattered precipitation throughout the East Coast. April 25th looks the most different in CTRL compared to the stage IV data, with the CTRL precipitation covering a smaller band than the more widespread precipitation observed. The precipitation on the 25th is also located further North in southern Missouri, whereas the stage IV precipitation covers a large portion of northern Arkansas. Also, overall, the location of the precipitation throughout the event matches well with where we would expect as the upper level trough and associated jet streak propagates eastward (Figure 1.2).

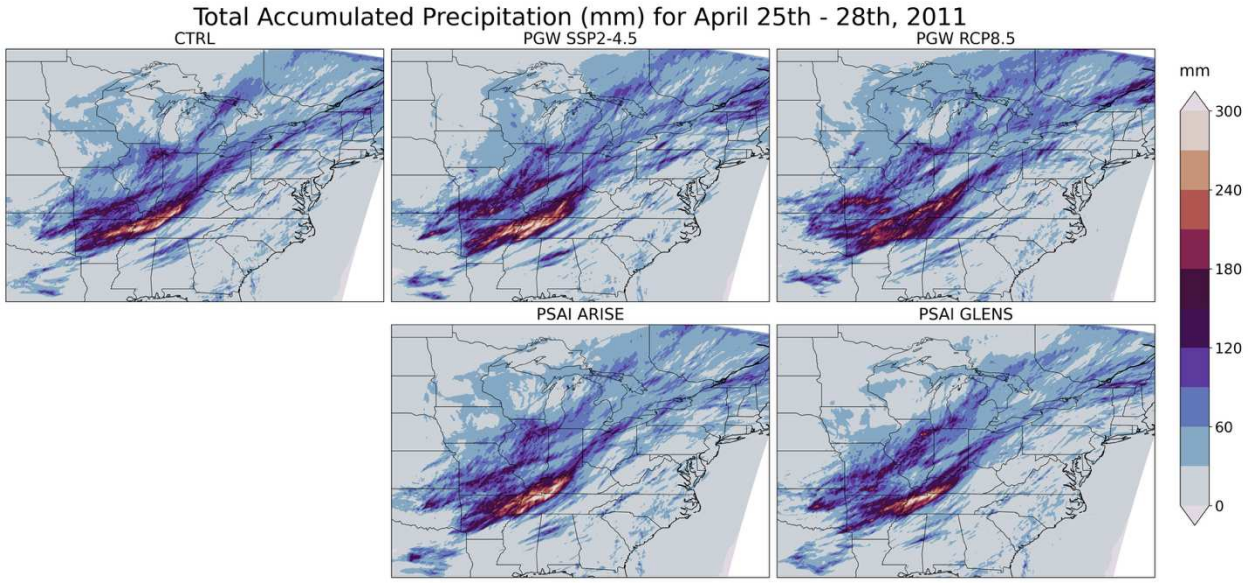

Figure 3.3: Simulated total accumulated precipitation (mm) over the 4 days of the 2011 Tornado Outbreak.

To consider the changes between the CTRL, PGW, and PSAI simulations, we first examine changes in temperature. The time series of the mean 2 m temperature during the event period is shown in Figure 3.2. There is an increase in surface temperatures under PGW SSP2-4.5 from CTRL, a larger increase in PGW RCP8.5, a slight increase in PSAI ARISE, and a slight decrease in PSAI GLENS. This pattern is the same as the trend seen in the surface temperature over the entire six months simulated, as in Sun et al. (2025). Sun et al. (2025) also note the fidelity with which the PGW and PSAI methods are able to replicate the vertical profiles of temperature compared to the original CESM experiments for these scenarios, in other words, the AOD delta term applied to the PSAI simulations provides a reasonable approximation of the radiational impacts of SAI. A notable feature of Figure 3.2 is the lack of change in the magnitude of the diurnal cycle. The average magnitude of the diurnal cycle ranges from 6.5 to 8.4˚C over the event, with the spread between individual simulations falling within 0.4˚C on average. A reduction in the difference between minimum and maximum daily surface temperature has been observed after volcanic eruptions (Robock, 2000) as a result of reducing incoming solar radiation. Since the

diurnal cycle of land surface temperature is known to have strong connections to the production of deep convection in North America (Tian et al., 2005), potential decreases in the amplitude of the diurnal cycle of temperature due to SAI could have important implications for severe storms. While there are slight differences in the diurnal cycle between the different simulations in Figure 3.2, the changes are not significantly large or consistent.

Returning to precipitation, the total accumulated precipitation of the event from the CTRL, PGW and PSAI simulations is shown in Figure 3.3. Qualitatively, both the PGW and the PSAI simulations produced a similar spatial structure to the CTRL simulation, with the region spanning from Arkansas through Tennessee and into Kentucky showing the most accumulated precipitation in all simulations. Other smaller precipitation patterns, such as a cluster of precipitation in Eastern Texas and a band of precipitation in Northern Alabama are also reproduced in all future simulations. This result is generally expected as the PGW and PSAI simulations are both grounded in the atmospheric reanalysis forcing (ERA5) with perturbations from future climate states added to the key variables as discussed in the Methods section.

While the general spatial structure and magnitude of accumulated precipitation shown in Figure 3.3 are similar, there are also some notable differences. The area with the highest accumulated rainfall is slightly larger in the PGW SSP2-4.5 and PSAI ARISE simulations, extending further East into Tennessee in PGW SSP2-4.5 and extending further North into Missouri and Illinois in PSAI ARISE. In the PSAI GLENS simulation this area is smaller, with less accumulated precipitation in Arkansas and Kentucky. This area is most changed in the PGW RCP8.5 simulation, where high precipitation extends in all directions, further into Missouri, Illinois, Indiana, and Tennessee than in the other simulations. Additionally, there is a notable decrease in the highest magnitude of precipitation in the area on the westernmost side of Tennessee

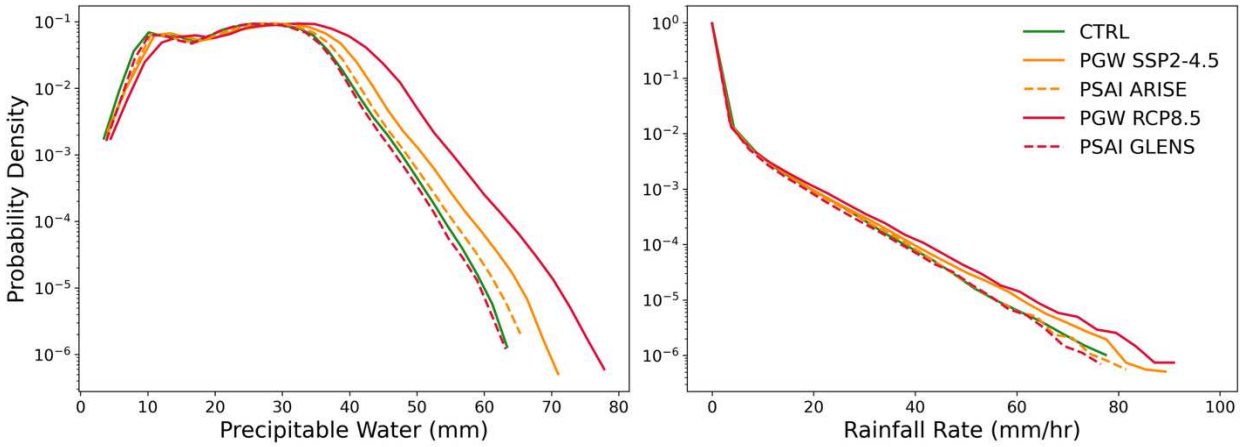

Figure 3.4: Histograms of precipitable water (mm, left) and rainfall rate (mm, right) over the event region and time period of the 2011 Tornado Outbreak.

and Kentucky in PGW RCP8.5 compared to the other simulations. Another interesting feature of both the PGW and PSAI simulations compared to CTRL is an increase in the scattered precipitation further North into Missouri. Further examination of spatial differences between simulations will be discussed later.

To further assess how precipitation and moisture may change in the future scenarios we explore, histograms of the hourly rainfall rate and precipitable water are shown in Figure 3.4. To produce this plot, the hourly data over the event region was first flattened, i.e. the data was reshaped into a one-dimensional array and any spatial or temporal information removed. Each data point was then weighted as a fraction of the total number of data points. Eighty equally sized bins were used to split the data, and bins containing fewer than ten data points were discarded. The populations of precipitable water show a clear increase in probability density for precipitable water at ~40 mm and higher from CTRL for both PGW simulations, although the increases are largest for PGW RCP8.5. This means that at every value of precipitable water of ~40 mm or more, there are more pixels in the PGW simulations experiencing that level of moisture during this event. Additionally, while the population of precipitable water for the CTRL simulation ends just after

60 mm, the populations of the PGW simulations both reach past 70 mm. PSAI simulations on the other hand have populations closer to that of CTRL, with PSAI ARISE having a slight increase in probability density from CTRL and PSAI GLENS having a slight decrease. The increase from CTRL in PSAI ARISE and decrease from CTRL in PSAI GLENS, as seen in both the 2 m temperature and precipitable water, is generally consistent with the target objectives of the ARISE and GLENS simulations. Recall that ARISE aimed to maintain the global mean temperature of approximately ~1.5˚C above preindustrial, representative of 2020-2039, whereas GLENS aimed to maintain the climate state of 2020 (approximated by 2015-2025, which is ~1.0˚C above preindustrial (Keys et al., 2022)). Thus, we would expect the PSAI GLENS simulation to represent the response of a climate with a global mean temperature that is cooler than that of PSAI ARISE, as we see here. Notably, Tilmes et al. (2018) observed a pattern of regional cooling over North America in the GLENS simulations, which may explain why the response of the PGW GLENS simulations in Fig. 6 is near or below that of the CTRL simulation. The populations of hourly rainfall rate are much closer in spread than those of precipitable water, but we still see an increase in intensity for the PGW simulations and magnitudes closer to that of CTRL for the PSAI simulations. Again, in the PGW simulations, the population extends to more extreme rainfall rates than in the CTRL or in the PSAI simulations. These results agree with previous work finding that convective precipitation and precipitation from mesoscale convective systems is expected to be enhanced in a warmer climate (E. M. Dougherty et al., 2023; Loriaux et al., 2013).

Also highly relevant metrics for the potential of severe weather are the thermodynamic variables CAPE and CIN. Low CIN (> -50 J kg^{-1}) and high CAPE in an environment allow for convection to be easily initiated, making it more unlikely that the convection will become severe. Large amounts of CIN (< -200 J kg^{-1}), on the other hand, may prevent convection from occurring

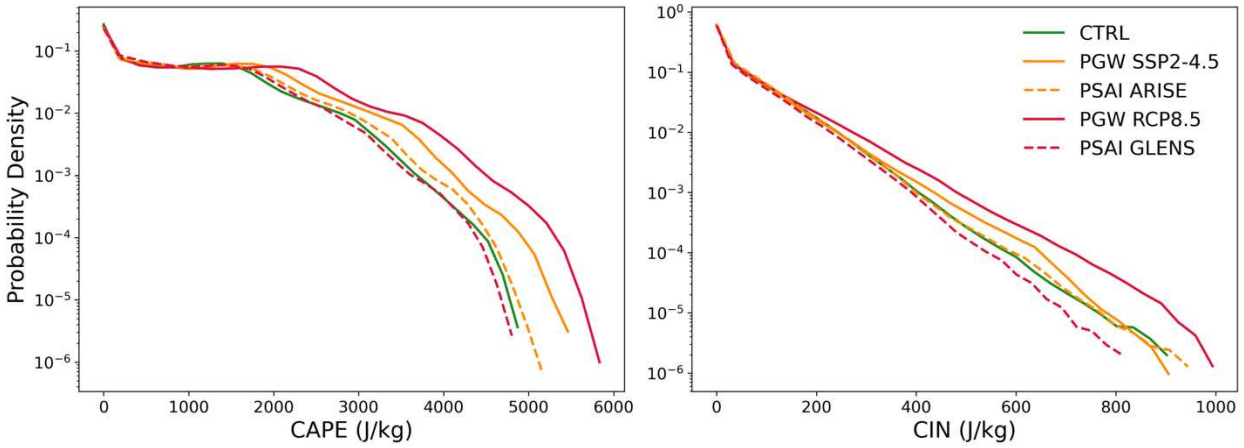

Figure 3.5: Histograms of thermodynamic variables CAPE (J kg^{-1}, left) and CIN (J kg^{-1}, right) over the event region and time period of the 2011 Tornado Outbreak.

even in an environment with high CAPE. However, environments with moderate CIN (-50 J kg^{-1} > CIN > -200 J kg^{-1}) can result in vigorous convection, provided that there is a buildup of CAPE and that convection can be initiated due to vertical lifting or strong surface heating. As with rainfall rate and precipitable water, changes in the populations of CAPE and CIN are assessed using histograms.

There are generally elevated amounts of CAPE and CIN in the PGW simulations compared to the CTRL (Figure 3.5), which is what we would expect under warmer and more moist conditions. This result also agrees with past assessments of CAPE and CIN under warmer future climates (Diffenbaugh et al., 2013; Franke et al., 2024; Glade et al., 2023; Hoogewind et al., 2017; K. L. Rasmussen et al., 2017; Trapp & Hoogewind, 2016). Additionally, the difference in CAPE and CIN between the CTRL and the PGW simulations increases near the tail of the distributions. One exception is in PGW SSP2-4.5, where at extreme values, the probability density returns to magnitudes closer to that of CTRL. For the PSAI simulations, populations of CAPE and CIN are consistently closer to that of the CTRL simulation, with the PSAI ARISE simulation being slightly

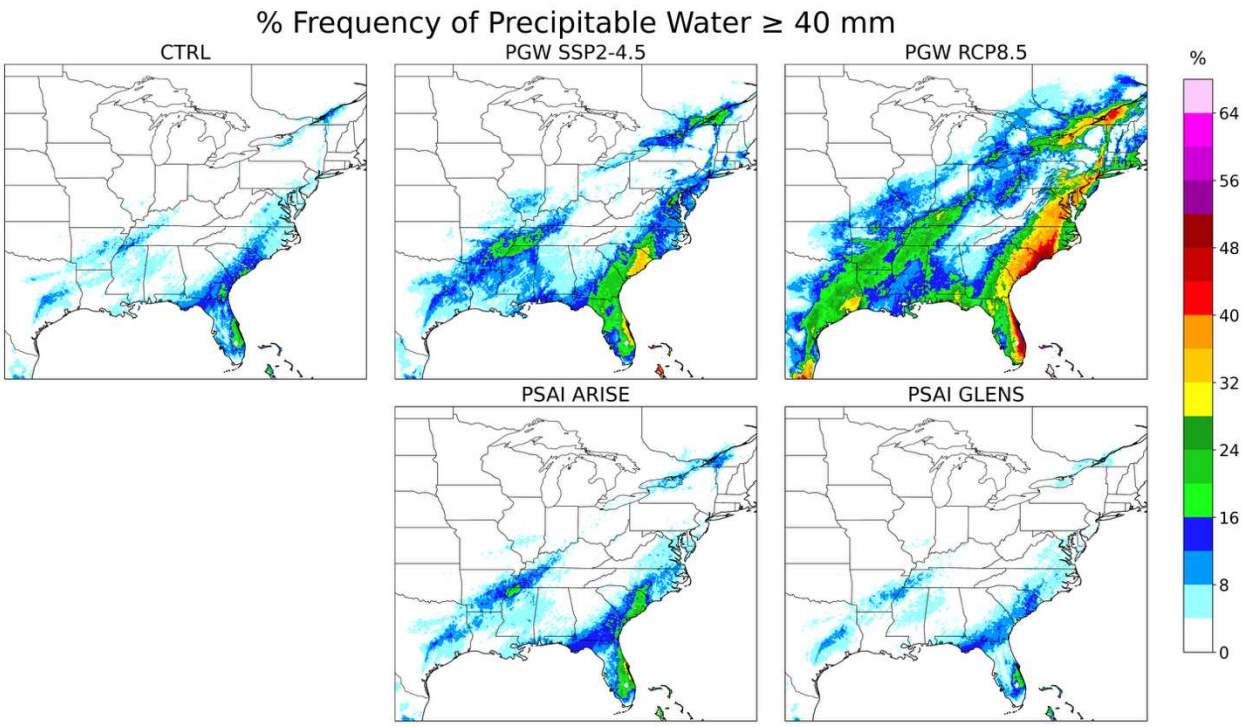

Figure 3.6: Percent frequency of the hourly timesteps that precipitable water exceeded 40 mm at each grid point during the event period.

increased from CTRL and the PSAI GLENS simulation being slightly decreased from CTRL similar to changes in the populations of precipitable water and rainfall rate.

To consider spatial changes in addition to changes in the total population of moisture, values of precipitable water exceeding 40 mm are analyzed over the event region. While 50 mm is often used as a threshold for extreme atmospheric moisture (NWS, 2010), we chose 40 mm for this analysis to make the change in spatial patterns more clear while still representing high levels of moisture. The frequency of the precipitable water at each grid point surpassing 40 mm during the event period is shown in Figure 3.6, following Eqn. 5. There is an increase in PGW simulations both in the spatial extent affected by high levels of moisture as well as in the frequency of the 40 mm threshold being breached. Especially in the region observed to have the most precipitation for this event, from Arkansas through Kentucky, there is a markedly larger area experiencing high

values of moisture. The frequency ≥ 40 mm of precipitable water is higher as well – in some parts of the area by up to 28%. This suggests that in a warmer climate, more areas could be subjected to extreme moisture and extreme moisture could be present for a longer duration during severe convective weather. In contrast, the PSAI simulations show spatial extents and magnitudes of precipitable water that are much closer to that of the CTRL simulation.

3.2 Reflectivity, Updraft Speed, and Updraft Helicity

Table 3.1: %Δ from CTRL in pixels exceeding reflectivity thresholds above 10 km in altitude in the event region and period. (simulation – CTRL / CTRL * 100)

Reflectivity Threshold	PGW SSP2-4.5	PGW RCP8.5	PSAI ARISE	PSAI GLENS
0+ dBZ > 10 km	14.09	22.78	3.22	-9.74
20+ dBZ > 10 km	16.24	26.84	6.12	-11.10
40+ dBZ > 10 km	95.49	230.45	9.02	-31.58

We also examine variables such as reflectivity, updraft speed, and updraft helicity – variables which are not well simulated in coarser resolution models and are important indicators of hazardous convection. Changes in reflectivity falling within specific thresholds at altitudes higher than 10 km are considered, since storm height is directly related to intensity. The percent change in the number of pixels in the storm region with reflectivities of 0, 20, and 40 dBZ or greater higher than 10 km in altitude in the PGW and PSAI simulations compared to that of the CTRL simulation is shown in Table 3.1. The percent change in these high altitude reflectivity counts for the PGW and PSAI simulations is consistent with previous results, with a moderate increase from CTRL in PGW SSP2-4.5, a stronger increase in PGW RCP8.5, a slight increase in PSAI ARISE, and a decrease in PSAI GLENS. Additionally, this change is amplified for

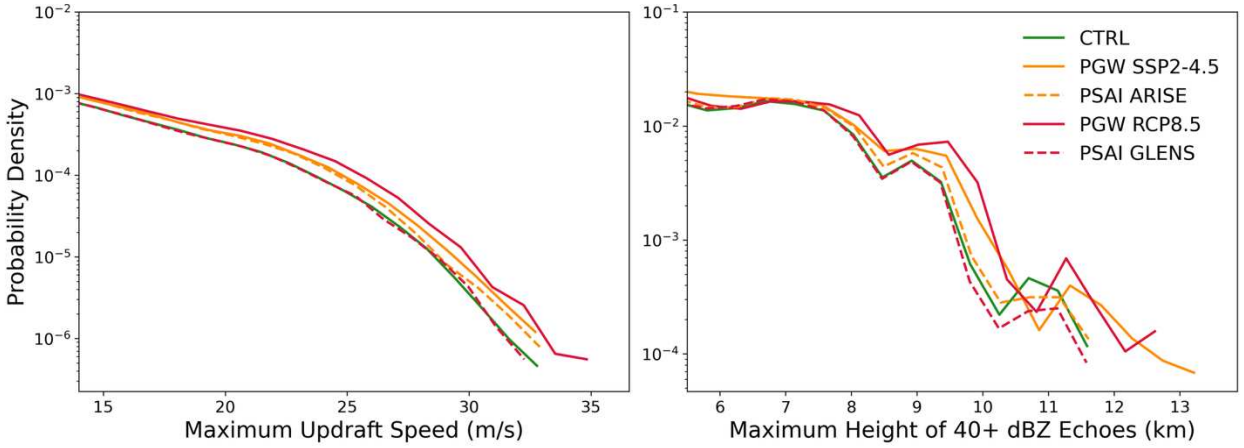

Figure 3.7: Histograms of maximum updraft speed (m s^{-1}, left) and maximum height of 40+ dBZ radar echoes (km, right) over the event region and period. Histograms are cutoff at 13 m s^{-1} and 5 km to draw attention to the character potentially indicative of severe weather.

reflectivities greater than 40 dBZ. While this is consistent with the response seen in the histograms of other variables, such as precipitable water, rainfall rate (Figure 3.4), and CAPE (Figure 3.5), it should be noted that 40+ dBZ echoes higher than 10 km are significantly less frequent compared to that of the 0 dBZ and 20 dBZ or greater echoes, which may also make the percent differences large. In general, these changes suggest that deep convective storm features could become more frequent in a future warmer climate, whereas in a future climate under SAI, the changes would be smaller.

Histograms of the height of reflectivity echoes ≥ 40 dBZ and the maximum updraft speed are assessed in Figure 3.7. Generally, these populations follow a similar change as previous results, where the PGW simulations are increased from CTRL and the PSAI simulations are similar to CTRL behavior. One deviation from this is in the PSAI ARISE simulation at high values of maximum updraft speed. Though the spread in these populations is somewhat small to begin with, the PSAI ARISE simulation is much closer to the PGW SSP2-4.5 simulation at extreme values of maximum updraft speed than to CTRL. In the populations of high altitude reflectivity echoes of 40 dBZ or greater, there is a notable peak in the CTRL and PSAI simulations around 11 km,

Table 3.2: Mean UH03 during the event period when exceeding the indicated threshold value.

UH03 (m^2 s^{-2})	CTRL	PGW SSP2-4.5	PGW RCP8.5	PSAI ARISE	PSAI GLENS
75	101.27	104.95	103.89	99.67	99.39
120	143.90	150.39	148.91	145.77	141.33

whereas in the PGW simulations this peak is shifted higher to ~11.5 km. This suggests that in a warmer future, storms with strong updrafts and high reflectivity values above 10 km may occur more frequently, which has implications for other dangerous storm characteristics such as hail production and lightning processes (Deierling & Petersen, 2008).

In addition to updraft speed and reflectivity, we consider UH03 as a metric for forecasting tornadic environments at values of 120 m^2 s^{-2} or greater and severe storm environments at values of 75 m^2 s^{-2} or greater (Sobash et al., 2016). In Sobash et al. (2016), UH03 > 120 m^2 s^{-2} showed the highest skill in predicting tornadic events. UH03 > 75 m^2 s^{-2} was found to have less skill in predicting tornadic events than UH03 > 120 m^2 s^{-2}, but significantly more skill than the thresholds tested of lower values, which is why we use it here to assess severe storm environments in general. Mean values of UH03 > 120 m^2 s^{-2} and 75 m^2 s^{-2} during the Super Tornado Outbreak of 2011 are shown in table 3.2. Compared to CTRL, there are increases in the mean value of the UH03 in the PGW simulations for both thresholds. For PSAI simulations, there is a decrease in the mean UH03 from CTRL in PSAI GLENS for both thresholds and for PSAI ARISE in the 75 m^2 s^{-2} threshold. PSAI ARISE shows a slight increase in the mean UH03 value for helicity exceeding the 120 m^2 s^{-2} threshold. While these results could indicate an increase in storm updraft rotation and tornadic potential in warmer futures and a decrease under SAI, the number of pixels that breached these thresholds were on the scale of 50-500. Specifically, PSAI simulations had pixels with UH03 > 120 m^2 s^{-2} on the order of 10^1 and UH03 > 75 m^2 s^{-2} on the order of 10^2. PGW simulations had

pixels with UH03 > 120 m^2 s^{-2} and UH03 > 75 m^2 s^{-2} on the order of 10^2. Furthermore, the populations of UH03 are examined and the spread between simulations was small also. While the results shown here suggest that rotating updrafts and tornadic potential may be more frequently achieved under global warming than in the historical climate conditions or under SAI, the small sample size found warrants further work considering supercell and tornado forecasting parameters in future climates. Furthermore, leveraging modelling studies that explicitly resolve tornadoes on very high spatial resolution would also help to better understand how tornados and tornadic environments may change in possible future climates.

Similar to our analysis of precipitable water, we also consider how the spatial distributions of maximum updraft speed > 5 m s^{-1} and reflectivity echoes ≥ 20 dBZ change under different future forcing scenarios. The percent frequency of the occurrence of 20+ dBZ echoes higher than 10 km and the difference from CTRL for the PGW and PSAI simulations is shown in Figure 3.8. The same plots for maximum updraft velocities greater than 5 m s^{-1} are shown in Figure 3.9. 20 dBZ echoes and 5 m s^{-1} maximum updraft velocity were chosen so that the frequency of occurrence was high enough to be able to see broad regions of the storm structures and spatial patterns while still indicating convective activity. Broadly speaking, we see similar increases and decreases in the PGW and PSAI simulations to what was observed in the histograms of these and other variables thus far. Additionally, the PGW SSP2-4.5 and PGW RCP8.5 simulations show increases in frequency over a larger area than the CTRL simulation, indicating that a larger area of storm systems like this one could be impacted by high intensity updrafts and reflectivity echoes in a warmer climate. Areas showing a decrease in frequency for PGW simulations could be due to the suppression of weaker convection due to future increases in CIN, or it could be due to slight shifts

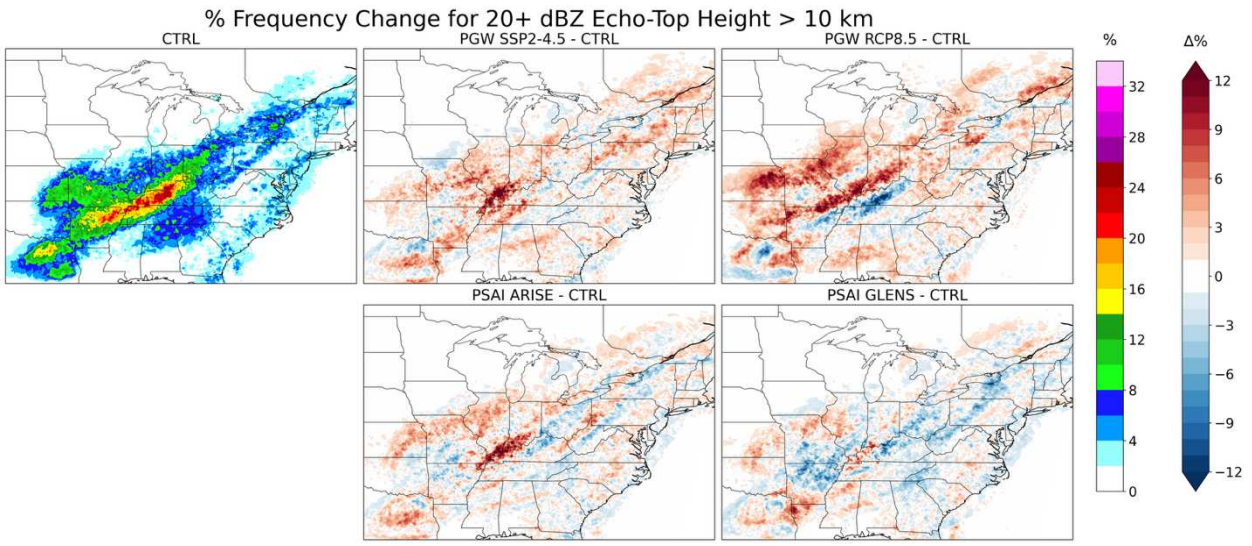

Figure 3.8: Percent frequency of the hourly timesteps for the occurrence of 20 dBZ or greater echo-top heights over 10 km and the change from CTRL in pixels within storm region over event period.

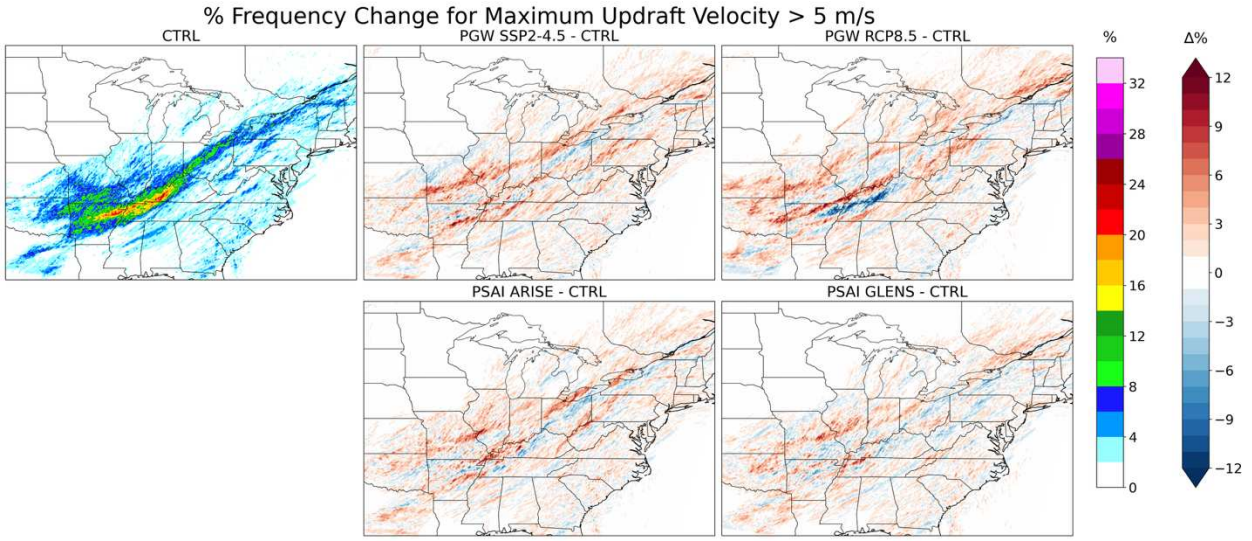

Figure 3.9: Percent frequency of the hourly timesteps for the occurrence of maximum updraft velocity greater than 5 m s^{-1} and the change from CTRL in pixels within storm region over event period.

in the location of convective features within simulations. For each simulation, the spatial pattern differences are consistent between reflectivity and maximum updraft speed.

To assess if the timing of the storm has changed, the mean hourly accumulated precipitation and the mean echo top height over the event period is depicted in Figure 3.10. Between the CTRL,

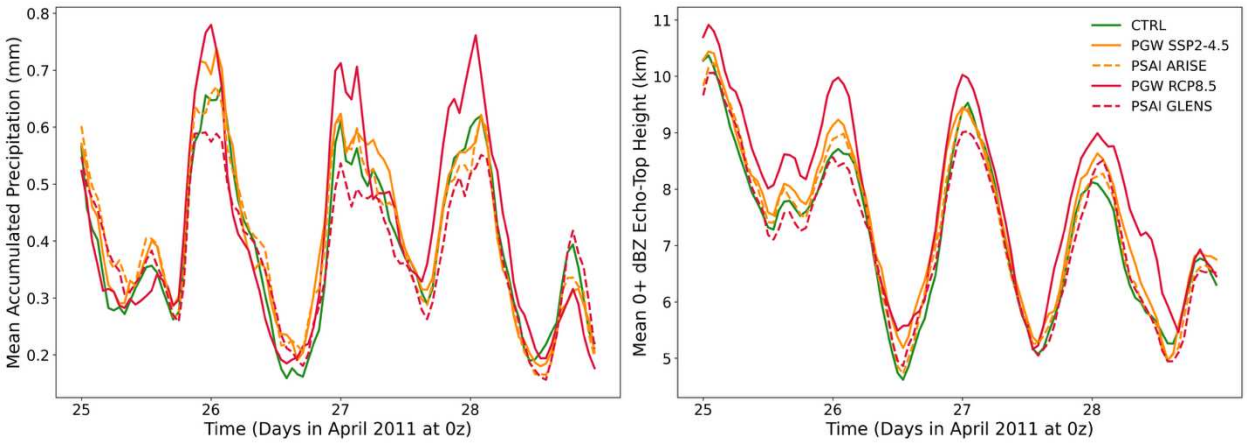

Figure 3.10: Time series of the mean accumulated precipitation (mm, left) and the mean echo-top height (at 0 dBZ, km, right), over the event region.

PGW, and PSAI simulations, there is little difference in the timing of each peak in precipitation or echo top height. In other words, the start, local maxima, and end of each peak don't shift earlier or later collectively. This result is consistent also with timing of 20+ and 40+ dBZ echo-top heights, not shown. There are, however, changes in the timing of individual peaks. For example, the peak precipitation for the PGW RCP8.5 simulation on April 27th has a large decrease followed by a smaller shoulder closer to the intensity of the precipitation in the other simulations. Furthermore, the precipitation and the echo-top height peaks for PGW RCP8.5 on April 28th are slightly broader than the peaks for the other simulations. Assessing the robustness of these changes would require analysis of the timing of these peaks for an ensemble of simulations, which is outside the scope of this study. Since the timing of these features are not changing dramatically or consistently on each day, it suggests that broadly, the timing of this storm would be unlikely to change in a future climate. The fact that there are changes in these peaks between simulations, however, indicates the need for further work examining changes in the timing and duration of hazardous convective weather in future climates.

3.3 Storm Modes

Finally, to understand changes in the life cycle and convective character of this storm, we analyze TRMM-heritage storm modes during this event. The criteria used to identify storm modes were intended to classify types of convective behavior that represent different stages in a storm's development. DCCs represent explosive and vigorous convection at the beginning of the lifecycle of a convective cell, WCCs represent intense convection that has organized into larger mesoscale units, and DWCCs represent a transitional phase between the two. Finally, BSRs represent a mature and well-developed mesoscale convective system, usually closer to the end of its life (Houze et al., 2007, 2015; Rasmussen & Houze, 2011, 2016; Romatschke & Houze, 2010). The changes in BSRs are not examined in this study because they are not as important as the other storm modes for describing potential changes in a tornado outbreak case. By characterizing precipitation systems into different storm modes, we are able to consider the implications for life cycle and the intensity of the storm in our case study under different future climates. We conduct similar analysis as with the other variables described previously by considering the spatial frequency as well as the frequency of occurrence for the storm modes.

Table 3.3 shows the percent change in the PGW and PSAI simulations from CTRL in the occurrence of each storm mode accumulated over the spatiotemporal extent of the 2011 Super Tornado Outbreak. Perhaps the most straightforward to understand are the changes in DWCCs, where we see an increase in the occurrence of DWCCs in PGW SSP2-4.5, a larger increase in PGW RCP8.5, a smaller increase in PSAI ARISE, and a small decrease in PSAI GLENS, similar to the response seen previously. This makes sense given that the variables analyzed thus far were chosen to consider convection and storm severity, and DWCCs represent the stage of convection where the storm is mature and still contains intense deep convection. Comparing this to the changes

Table 3.3: %Δ from CTRL in pixels exceeding reflectivity thresholds above 10 km in altitude in the event region and period. (simulation – CTRL / CTRL * 100)

Storm Mode	PGW SSP2-4.5	PGW RCP8.5	PSAI ARISE	PSAI GLENS
DCC	3.54	-8.62	6.03	-2.86
DWCC	16.06	34.83	10.68	-0.46
WCC	14.06	36.78	-28.25	-14.15

seen in the occurrence of DCCs, it's initially unintuitive why PGW RCP8.5 would have a decrease in DCC occurrence, as well as why PSAI ARISE would have a higher occurrence of DCCs than PGW SSP2-4.5. DCCs represent young convective activity, or isolated instances of > 40 dBZ over 10 km in height. We saw previously that PGW RCP8.5 had increased instances of > 40 dBZ over 10 km in height than PGW SSP2-4.5. This difference between the populations of DCCs and > 40 dBZ over 10 km in PGW RCP8.5 compared to CTRL may be accounted for by considering that some instances of reflectivity > 40 dBZ over 10 km are classified as DWCCs. As a reminder, DWCCs are identified as WCCs with at least one instance of a DCC within the WCC. It follows that there could be a decrease in DCCs, as long as it is paired with a substantial increase in DWCCs, which is what we see. Furthermore, the percent change for DCCs is relatively small, so it's possible that this signal would change in a different model realization of this storm.

When considering the WCCs, there is an increase in the occurrence of WCCs in PGW simulations, and a decrease in occurrence in PSAI simulations. It's important to note, however, that there are relatively few WCCs compared to DWCCs. This is likely explained by the severity of the event chosen; not many pixels were identified as WCCs because they instead fell into the DWCC category due to the presence of a DCC within the area. Specifically, compared to the magnitude of pixels identified as DWCCs, the number of pixels identified as WCCs were 2 orders

of magnitude smaller, and the number of pixels identified as DCCs was 1 order of magnitude smaller. Since the changes seen in each storm mode for these simulations are intrinsically connected to the convective nature of this event, this analysis would be best considered in

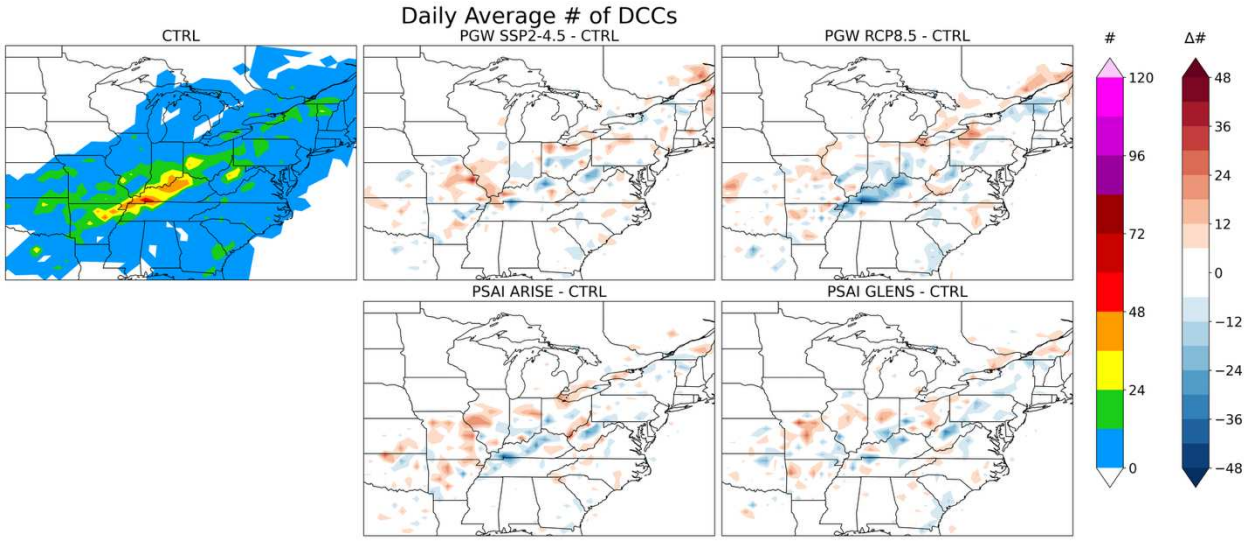

Figure 3.11: Daily average number of DCCs occurring in a 60x60 km pixel for the CTRL simulation, or the change in the daily average number for the PGW and PSAI simulations within storm region over the event period.

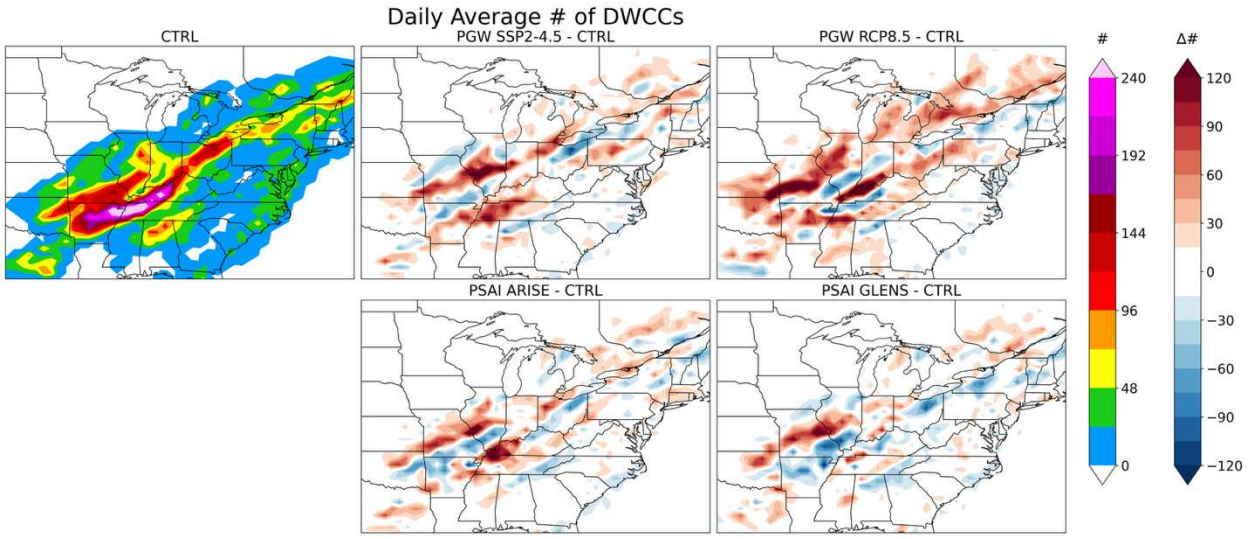

Figure 3.12: Daily average number of DWCCs occurring in a 60x60 km pixel for the CTRL simulation, or the change in the daily average number for the PGW and PSAI simulations within storm region over the event period.

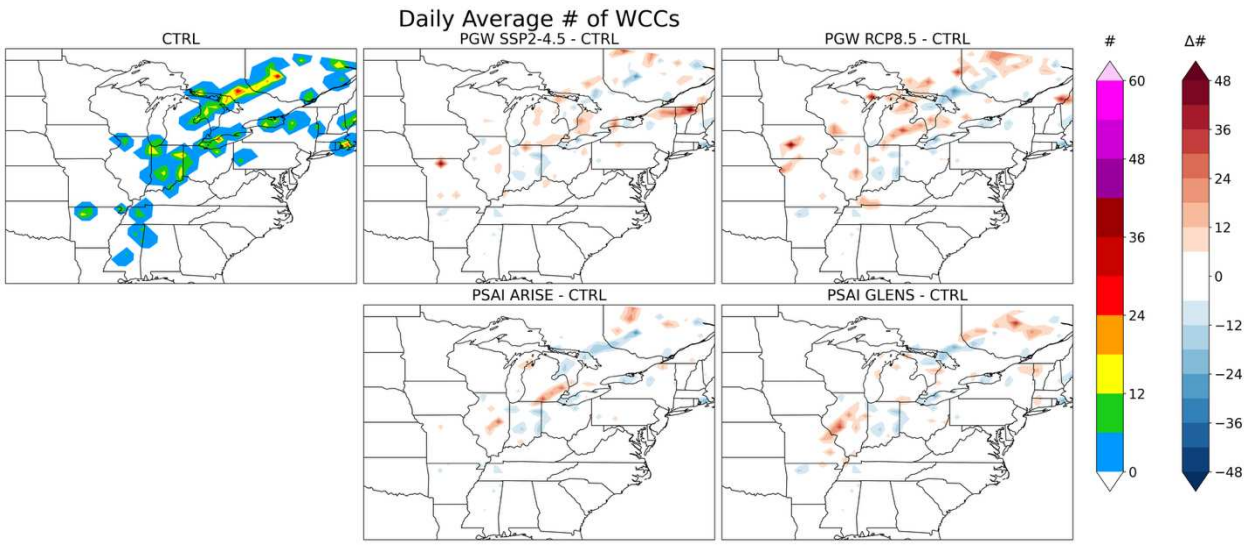

Figure 3.13: Daily average number of WCCs occurring in a 60x60 km pixel for the CTRL simulation, or the change in the daily average number for the PGW and PSAI simulations within storm region over the event period.

comparison to assessment of storm modes in other case studies as well, to provide a more holistic sense of potential changes in convective life cycles in different types of storms in future climates.

We also examine changes in the spatial distributions of storm modes. The daily average number of DCCs occurring in each grid cell during the event is shown in Figure 3.11. The data was regridded into 60 km grid cells to smooth the contours and make the spatial patterns more clear, as is consistent with other studies (Romatschke & Houze, 2010). The same data as Figure 3.11 is shown in Figures 3.12 and 3.13 for DWCCs and WCCs. Broadly there are similar changes in the spatial frequency to the percent change in occurrence. Notably, the occurrence of DWCCs and BSRs are much higher than that of DCCs and WCCs, making the changes in spatial patterns from the CTRL to the PGW or PSAI simulations more clear. As seen with the other spatial frequency plots, there is a notable intensification and a larger area experiencing DWCCs in PGW RCP8.5 compared to CTRL. Furthermore, bands of increase or decrease in DWCC occurrence also agree with the spatial frequency patterns of the other mesoscale variables shown prior. The

changes in the occurrence of DCCs in PGW and PSAI simulations compared to CTRL are small and are spatially scattered, making interpretation difficult. One exception is an area of decreased DCC occurrence along the northwestern border of Kentucky in the PGW RCP8.5 simulation. This is co-located with both the most active area for DCCs and DWCCs in the CTRL run. There is also an area of increase in DWCC occurrence in the PGW RCP8.5 simulation very close to this location. This seems to support the hypothesis stated earlier that a significant amount of DCC character for PGW RCP8.5 is likely found in the population of DWCCs. Similarly, the low number of occurrences of WCCs along with the scattered spatial pattern supports the idea that most WCCs for this event likely fall into the DWCC category due to the high convective activity of this storm system.

CHAPTER 4

DISCUSSION AND CONCLUSIONS

The analysis described herein is performed on novel convection-permitting simulations of hazardous convective weather in different future climate scenarios under global warming and SAI. The simulations by Sun et al (2025) are used to assess the potential impacts of global warming and SAI on the 2011 Super Tornado Outbreak. This study with the study by Sun et al (2025) are the first that we know of to examine convective weather under SAI using km-scale simulations with direct shortwave radiation reductions. The impact of ensemble mean climatic forcing from SSP2-4.5, RCP8.5, ARISE-SAI, and GLENS on variables indicative of hazardous convective weather in 2060-2069 was considered. The key conclusions from this study are as follows:

- Parameters indicating storm severity, including precipitable water, rainfall rate, CAPE, maximum updraft speed, the maximum height of reflectivity echoes ≥ 40 dBZ, and UH03, increased in the PGW simulations but were closer to CTRL in the PSAI simulations.
- Histograms of the variables precipitable water, rainfall rate, CAPE, and the maximum height of 40+ dBZ echoes show that PGW simulations achieve more extreme values of these variables than in either the CTRL or PSAI simulations.
- A larger area is impacted by precipitable water ≥ 40 mm, maximum updraft speeds > 5 m s^{-1}, and reflectivity echoes ≥ 20 dBZ in PGW simulations than in the CTRL or PSAI simulations.
- The timing of peak convection or precipitation did not change appreciably between CTRL, PGW, or PSAI simulations, though further study of the timing of convection in future climates is warranted.

- PGW simulations show substantial increases in DWCCs compared to CTRL or PSAI, further emphasizing the changes in convective intensity and convective organization for the 2011 Super Tornado Outbreak.

A limitation of these simulations is that they represent one model realization of one case study. Analysis of an ensemble of simulations of convective weather in future climates will be necessary to examine the potential range and uncertainty of variables examined here due to the impacts of internal climate variability. Additionally, examination of case studies representing different archetypes of convective weather is necessary to continue to assess how hazardous convective weather may change in future climates, since different types of storms may respond differently to the same climatic forcing.

This study with the study by Sun et al. (2025) are the first to examine how hazardous convective weather may change in a future climate under global warming and SAI using a convection permitting model. We find that for the Super Tornado Outbreak of 2011, where the changes under global warming may intensify storm severity, the radiational changes from the implementation of SAI may keep the intensity closer to the historical level. This work has assessed many variables, including precipitable water, rainfall rate, CAPE, CIN, updraft speed, reflectivity, updraft helicity, and storm modes, which are important indicators of storm intensity, providing a number of different possible methods of analysis to assess changes in case studies of hazardous convective weather in the future. While a singular study cannot answer all of the questions we may have on how SAI may impact future weather, this marks an important starting place for research on this subject. As discussions relating to both how hazardous convective weather may change in a future climate and the potential for SAI deployment continue, this study, and other studies like

it, will provide important scientific background to help both policymakers and the public understand the potential impacts SAI may have.

REFERENCES

Allen, M. R., & Ingram, W. J. (2002). Constraints on future changes in climate and the hydrologic cycle. *Nature, 419*(6903), 224–232. https://doi.org/10.1038/nature01092.

Ban, N., Schmidli, J., & Schär, C. (2015). Heavy precipitation in a changing climate: Does short-term summer precipitation increase faster? *Geophysical Research Letters, 42*(4), 1165–1172. https://doi.org/10.1002/2014GL062588.

Barnes, E. A., Hurrell, J. W., & Sun, L. (2022). Detecting Changes in Global Extremes Under the GLENS-SAI Climate Intervention Strategy. *Geophysical Research Letters, 49*(20), e2022GL100198. https://doi.org/10.1029/2022GL100198.

Bednarz, E. M., Visioni, D., Richter, J. H., Butler, A. H., & MacMartin, D. G. (2022). Impact of the Latitude of Stratospheric Aerosol Injection on the Southern Annular Mode. *Geophysical Research Letters, 49*(19), e2022GL100353. https://doi.org/10.1029/2022GL100353.

Brooks, H. E. (2013). Severe thunderstorms and climate change. *Atmospheric Research, 123*, 129–138. https://doi.org/10.1016/j.atmosres.2012.04.002.

Brooks, Harold E. (2007). Ingredients-Based Forecasting. In D. B. Giaiotti, R. Steinacker, & F. Stel (Eds.), *Atmospheric Convection: Research and Operational Forecasting Aspects* (pp. 133–140). Vienna: Springer Vienna. https://doi.org/10.1007/978-3-211-69291-2_12.

Buck, H. J. (2022). Environmental Peacebuilding and Solar Geoengineering. *Frontiers in Climate, 4*. https://doi.org/10.3389/fclim.2022.869774.

Burgess, M. G., Ritchie, J., Shapland, J., & Pielke, R. (2020). IPCC baseline scenarios have over-projected CO2 emissions and economic growth. *Environmental Research Letters, 16*(1), 014016. https://doi.org/10.1088/1748-9326/abcdd2.

Carroll-Smith, D., Trapp, R. J., & Done, J. M. (2021). Exploring Inland Tropical Cyclone Rainfall and Tornadoes under Future Climate Conditions through a Case Study of Hurricane Ivan. *Journal of Applied Meteorology and Climatology, 60*(1), 103–118. https://doi.org/10.1175/JAMC-D-20-0090.1.

Chasteen, M. B., & Koch, S. E. (2022). Multiscale Aspects of the 26–27 April 2011 Tornado Outbreak. Part I: Outbreak Chronology and Environmental Evolution. *Monthly Weather Review, 150*(2), 309–335. https://doi.org/10.1175/MWR-D-21-0013.1.

Dai, A. (2006). Precipitation Characteristics in Eighteen Coupled Climate Models. *Journal of Climate, 19*(18), 4605–4630. https://doi.org/10.1175/JCLI3884.1.

Dai, A., & Trenberth, K. E. (2004). The Diurnal Cycle and Its Depiction in the Community Climate System Model. *Journal of Climate, 17*(5), 930–951. https://doi.org/10.1175/1520-0442(2004)017<0930:TDCAID>2.0.CO;2.

Dai, A., Rasmussen, R. M., Liu, C., Ikeda, K., & Prein, A. F. (2020). A new mechanism for warm-season precipitation response to globalwarming based on convection-permitting simulations. *Climate Dynamics, 55*(1), 343–368. https://doi.org/10.1007/s00382-017-3787-6.

Danabasoglu, G., Lamarque, J.-F., Bacmeister, J., Bailey, D. A., DuVivier, A. K., Edwards, J., et al. (2020). The Community Earth System Model Version 2 (CESM2). *Journal of Advances in Modeling Earth Systems, 12*(2), e2019MS001916. https://doi.org/10.1029/2019MS001916.

Deierling, W., & Petersen, W. A. (2008). Total lightning activity as an indicator of updraft characteristics. *Journal of Geophysical Research: Atmospheres, 113*(D16). https://doi.org/10.1029/2007JD009598.

Deser, C., Phillips, A., Bourdette, V., & Teng, H. (2012). Uncertainty in climate change projections: the role of internal variability. *Climate Dynamics, 38*(3), 527–546. https://doi.org/10.1007/s00382-010-0977-x.

Diffenbaugh, N. S., Scherer, M., & Trapp, R. J. (2013). Robust increases in severe thunderstorm environments in response to greenhouse forcing. *Proceedings of the National Academy of Sciences, 110*(41), 16361–16366. https://doi.org/10.1073/pnas.1307758110.

Doswell, C. A., & Rasmussen, E. N. (1994). The Effect of Neglecting the Virtual Temperature Correction on CAPE Calculations. *Weather and Forecasting, 9*(4), 625–629. https://doi.org/10.1175/1520-0434(1994)009<0625:TEONTV>2.0.CO;2.

Dougherty, E., & Rasmussen, K. L. (2020). Changes in Future Flash Flood–Producing Storms in the United States. *Journal of Hydrometeorology, 21*(10), 2221–2236. https://doi.org/10.1175/JHM-D-20-0014.1.

Dougherty, E. M., Prein, A. F., Gutmann, E. D., & Newman, A. J. (2023). Future Simulated Changes in Central U.S. Mesoscale Convective System Rainfall Caused by Changes in Convective and Stratiform Structure. *Journal of Geophysical Research: Atmospheres, 128*(4), e2022JD037537. https://doi.org/10.1029/2022JD037537.

Du, J. (2011). NCEP/EMC 4KM Gridded Data (GRIB) Stage IV Data. Version 1.0 (Version 1.0) [GRIB-2: Gridded Binary Edition 2 (GRIB)]. UCAR/NCAR - Earth Observing Laboratory. https://doi.org/10.5065/D6PG1QDD.

Ekström, M., Grose, M. R., & Whetton, P. H. (2015). An appraisal of downscaling methods used in climate change research. *WIREs Climate Change, 6*(3), 301–319. https://doi.org/10.1002/wcc.339.

Franke, M. E., Hurrell, J. W., Rasmussen, K. L., & Sun, L. (2024). Impacts of forced and internal climate variability on changes in convective environments over the eastern United States. *Frontiers in Climate, 6,* 1385527. https://doi.org/10.3389/fclim.2024.1385527.

Glade, I., Hurrell, J. W., Sun, L., & Rasmussen, K. L. (2023). Assessing the Impact of Stratospheric Aerosol Injection on US Convective Weather Environments. *Earth's Future, 11*(12), e2023EF004041. https://doi.org/10.1029/2023EF004041.

Gutmann, E. D., Rasmussen, R. M., Liu, C., Ikeda, K., Bruyere, C. L., Done, J. M., et al. (2018). Changes in Hurricanes from a 13-Yr Convection-Permitting Pseudo–Global Warming Simulation. *Journal of Climate, 31*(9), 3643–3657. https://doi.org/10.1175/JCLI-D-17-0391.1.

Guyer, J. L. (2006). Cool season significant (F2-F5) tornadoes in the Gulf Coast states. Retrieved from https://www.semanticscholar.org/paper/Cool-season-significant-(F2-F5)-tornadoes-in-the-Guyer/7b48cf98aa0b465c6ef427216a0b8be99320730e.

Haberlie, A. M., Ashley, W. S., Battisto, C. M., & Gensini, V. A. (2022). Thunderstorm Activity Under Intermediate and Extreme Climate Change Scenarios. *Geophysical Research Letters, 49*(14), e2022GL098779. https://doi.org/10.1029/2022GL098779.

Hausfather, Z., & Peters, G. P. (2020). Emissions – the 'business as usual' story is misleading. *Nature, 577*(7792), 618–620. https://doi.org/10.1038/d41586-020-00177-3.

Hersbach, H., Bell, B., Berrisford, P., Hirahara, S., Horányi, A., Muñoz-Sabater, J., et al. (2020). The ERA5 global reanalysis. *Quarterly Journal of the Royal Meteorological Society, 146*(730), 1999–2049. https://doi.org/10.1002/qj.3803.

Hong, S.-Y., Noh, Y., & Dudhia, J. (2006). A New Vertical Diffusion Package with an Explicit Treatment of Entrainment Processes. *Monthly Weather Review, 134*(9), 2318–2341. https://doi.org/10.1175/MWR3199.1.

Hoogewind, K. A., Baldwin, M. E., & Trapp, R. J. (2017). The Impact of Climate Change on Hazardous Convective Weather in the United States: Insight from High-Resolution Dynamical Downscaling. *Journal of Climate, 30*(24), 10081–10100. https://doi.org/10.1175/JCLI-D-16-0885.1.

Houghton, H. G. (1968). On Precipitation Mechanisms and their Artificial Modification. *Journal of Applied Meteorology and Climatology, 7*(5), 851–859. https://doi.org/10.1175/1520-0450(1968)007<0851:OPMATA>2.0.CO;2.

Houze, R. A., Wilton, D. C., & Smull, B. F. (2007). Monsoon convection in the Himalayan region as seen by the TRMM Precipitation Radar. *Quarterly Journal of the Royal Meteorological Society, 133*(627), 1389–1411. https://doi.org/10.1002/qj.106.

Houze, R. A., Rasmussen, K. L., Zuluaga, M. D., & Brodzik, S. R. (2015). The variable nature of convection in the tropics and subtropics: A legacy of 16 years of the Tropical Rainfall Measuring Mission satellite. *Reviews of Geophysics, 53*(3), 994–1021. https://doi.org/10.1002/2015RG000488.

Houze, R. A., Wang, J., Fan, J., Brodzik, S., & Feng, Z. (2019). Extreme Convective Storms Over High-Latitude Continental Areas Where Maximum Warming Is Occurring. *Geophysical Research Letters, 46*(7), 4059–4065. https://doi.org/10.1029/2019GL082414.

Houze, R. A. (1994). *Cloud Dynamics* (Vol. 53). San Diego, CA: Academic Press.

Hueholt, D. M., Barnes, E. A., Hurrell, J. W., Richter, J. H., & Sun, L. (2023). Assessing Outcomes in Stratospheric Aerosol Injection Scenarios Shortly After Deployment. *Earth's Future, 11*(5), e2023EF003488. https://doi.org/10.1029/2023EF003488.

Hueholt, D. M., Barnes, E. A., Hurrell, J. W., & Morrison, A. L. (2024). Speed of environmental change frames relative ecological risk in climate change and climate intervention scenarios. *Nature Communications, 15*(1), 3332. https://doi.org/10.1038/s41467-024-47656-z.

Iacono, M. J., Delamere, J. S., Mlawer, E. J., Shephard, M. W., Clough, S. A., & Collins, W. D. (2008). Radiative forcing by long-lived greenhouse gases: Calculations with the AER radiative transfer models. *Journal of Geophysical Research: Atmospheres, 113*(D13). https://doi.org/10.1029/2008JD009944.

Ji, D., Fang, S., Curry, C. L., Kashimura, H., Watanabe, S., Cole, J. N. S., et al. (2018). Extreme temperature and precipitation response to solar dimming and stratospheric aerosol geoengineering. *Atmospheric Chemistry and Physics, 18*(14), 10133–10156. https://doi.org/10.5194/acp-18-10133-2018.

Johns, R. H., & Doswell, C. A. (1992). Severe Local Storms Forecasting. *Weather and Forecasting, 7*(4), 588–612. https://doi.org/10.1175/1520-0434(1992)007<0588:SLSF>2.0.CO;2.

Kain, J. S., Weiss, S. J., Bright, D. R., Baldwin, M. E., Levit, J. J., Carbin, G. W., et al. (2008). Some Practical Considerations Regarding Horizontal Resolution in the First Generation of Operational Convection-Allowing NWP. *Weather and Forecasting, 23*(5), 931–952. https://doi.org/10.1175/WAF2007106.1.

Keys, P. W., Barnes, E. A., Diffenbaugh, N. S., Hurrell, J. W., & Bell, C. M. (2022). Potential for perceived failure of stratospheric aerosol injection deployment. *Proceedings of the National Academy of Sciences, 119*(40), e2210036119. https://doi.org/10.1073/pnas.2210036119.

Knupp, K. R., Murphy, T. A., Coleman, T. A., Wade, R. A., Mullins, S. A., Schultz, C. J., et al. (2014). Meteorological Overview of the Devastating 27 April 2011 Tornado Outbreak. *Bulletin of the American Meteorological Society, 95*(7), 1041–1062. https://doi.org/10.1175/BAMS-D-11-00229.1.

Lee, W. R., MacMartin, D. G., Visioni, D., Kravitz, B., Chen, Y., Moore, J. C., et al. (2023). High-Latitude Stratospheric Aerosol Injection to Preserve the Arctic. *Earth's Future, 11*(1), e2022EF003052. https://doi.org/10.1029/2022EF003052.

Lenton, T. M., & Vaughan, N. E. (2009). The radiative forcing potential of different climate geoengineering options. *Atmospheric Chemistry and Physics, 9*(15), 5539–5561. https://doi.org/10.5194/acp-9-5539-2009.

Liu, C., Ikeda, K., Rasmussen, R., Barlage, M., Newman, A. J., Prein, A. F., et al. (2017). Continental-scale convection-permitting modeling of the current and future climate of North America. *Climate Dynamics, 49*(1), 71–95. https://doi.org/10.1007/s00382-016-3327-9.

Liu, C., Ikeda, K., & Rasmussen, R. (2024). Severe Convective Weather in the Central and Eastern United States: Present and Future. *Atmosphere, 15*(12), 1444. https://doi.org/10.3390/atmos15121444.

Long, J. C. S., & Shepherd, J. G. (2014). The Strategic Value of Geoengineering Research. In B. Freedman (Ed.), *Global Environmental Change* (pp. 757–770). Dordrecht: Springer Netherlands. https://doi.org/10.1007/978-94-007-5784-4_24.

Loriaux, J. M., Lenderink, G., Roode, S. R. D., & Siebesma, A. P. (2013). Understanding Convective Extreme Precipitation Scaling Using Observations and an Entraining Plume Model. *Journal of the Atmospheric Sciences, 70*(11), 3641–3655. https://doi.org/10.1175/JAS-D-12-0317.1.

Minnis, P., Harrison, E. F., Stowe, L. L., Gibson, G. G., Denn, F. M., Doelling, D. R., & Smith, W. L. (1993). Radiative Climate Forcing by the Mount Pinatubo Eruption. *Science, 259*(5100), 1411–1415.

Morrison, A. L., Pathak, D., Barnes, E. A., & Hurrell, J. W. (2024). Projected changes to Arctic shipping routes after stratospheric aerosol deployment in the ARISE-SAI scenarios. *Frontiers in Climate, 6*. https://doi.org/10.3389/fclim.2024.1426679.

National Academies of Sciences, E., and Medicine. (2021). *Reflecting Sunlight: Recommendations for Solar Geoengineering Research and Research Governance*. Washington, DC: The National Academies Press. https://doi.org/10.17226/25762.

NCEI. (2025). U.S. Billion-dollar Weather and Climate Disasters. Retrieved April 2, 2025, from https://www.ncei.noaa.gov/archive/accession/0209268.

Niu, G.-Y., Yang, Z.-L., Mitchell, K. E., Chen, F., Ek, M. B., Barlage, M., et al. (2011). The community Noah land surface model with multiparameterization options (Noah-MP): 1. Model description and evaluation with local-scale measurements. *Journal of Geophysical Research: Atmospheres, 116*(D12). https://doi.org/10.1029/2010JD015139.

NOAA. (2021, April 26). Revisiting the April 2011 Tornado “Super Outbreak” from Orbit. Retrieved April 1, 2025, from https://www.nesdis.noaa.gov/news/revisiting-the-april-2011-tornado-super-outbreak-orbit.

NWS. (2010, August 14). Near Record Precipitable Water Values. Retrieved April 9, 2025, from https://www.weather.gov/bmx/weatherreview_08142010.

O’Neill, B. C., Tebaldi, C., van Vuuren, D. P., Eyring, V., Friedlingstein, P., Hurtt, G., et al. (2016). The Scenario Model Intercomparison Project (ScenarioMIP) for CMIP6. *Geoscientific Model Development, 9*(9), 3461–3482. https://doi.org/10.5194/gmd-9-3461-2016.

Panasawatwong, W., Rasmussen, K. L., & Bell, M. M. (2022). A Climatology of Extreme Convective Storms in Tropical and Subtropical East Asia and Their Ingredients for Heavy Rainfall as Seen by TRMM. *Journal of Geophysical Research: Atmospheres, 127*(24), e2022JD036863. https://doi.org/10.1029/2022JD036863.

Rasmussen, K. L., & Houze, R. A. (2016). Convective Initiation near the Andes in Subtropical South America. *Monthly Weather Review, 144*(6), 2351–2374. https://doi.org/10.1175/MWR-D-15-0058.1.

Rasmussen, K. L., Prein, A. F., Rasmussen, R. M., Ikeda, K., & Liu, C. (2017). Changes in the convective population and thermodynamic environments in convection-permitting regional climate simulations over the United States. *Climate Dynamics, 55*(1), 383–408. https://doi.org/10.1007/s00382-017-4000-7.

Rasmussen, Kristen L., & Houze, R. A. (2011). Orogenic Convection in Subtropical South America as Seen by the TRMM Satellite. *Monthly Weather Review, 139*(8), 2399–2420. https://doi.org/10.1175/MWR-D-10-05006.1.

Rasmussen, R., Liu, C., Ikeda, K., Gochis, D., Yates, D., Chen, F., et al. (2011). High-Resolution Coupled Climate Runoff Simulations of Seasonal Snowfall over Colorado: A Process Study of Current and Warmer Climate. *Journal of Climate, 24*(12), 3015–3048. https://doi.org/10.1175/2010JCLI3985.1.

Rasmussen, R., Ikeda, K., Liu, C., Gochis, D., Clark, M., Dai, A., et al. (2014). Climate Change Impacts on the Water Balance of the Colorado Headwaters: High-Resolution Regional Climate Model Simulations. *Journal of Hydrometeorology, 15*(3), 1091–1116. https://doi.org/10.1175/JHM-D-13-0118.1.

Reboita, M. S., Gabriel Martins Ribeiro, J., Machado Crespo, N., da Rocha, R. P., Odoulami, R. C., Sawadogo, W., & Moore, J. (2024). Response of the Southern Hemisphere extratropical cyclone climatology to climate intervention with stratospheric aerosol injection. *Environmental Research: Climate, 3*(3), 035006. https://doi.org/10.1088/2752-5295/ad519e.

Richter, J. H., Visioni, D., MacMartin, D. G., Bailey, D. A., Rosenbloom, N., Dobbins, B., et al. (2022). Assessing Responses and Impacts of Solar climate intervention on the Earth system with stratospheric aerosol injection (ARISE-SAI): protocol and initial results from the first simulations. *Geoscientific Model Development, 15*(22), 8221–8243. https://doi.org/10.5194/gmd-15-8221-2022.

Robock, A. (2000). Volcanic eruptions and climate. *Reviews of Geophysics, 38*(2), 191–219. https://doi.org/10.1029/1998RG000054.

Romatschke, U., & Houze, R. A. (2010). Extreme Summer Convection in South America. *Journal of Climate, 23*(14), 3761–3791. https://doi.org/10.1175/2010JCLI3465.1.

Schär, C., Frei, C., Lüthi, D., & Davies, H. C. (1996). Surrogate climate-change scenarios for regional climate models. *Geophysical Research Letters, 23*(6), 669–672. https://doi.org/10.1029/96GL00265.

Schmidt, A., Mills, M. J., Ghan, S., Gregory, J. M., Allan, R. P., Andrews, T., et al. (2018). Volcanic Radiative Forcing From 1979 to 2015. *Journal of Geophysical Research: Atmospheres, 123*(22), 12491–12508. https://doi.org/10.1029/2018JD028776.

Seeley, J. T., & Romps, D. M. (2015). The Effect of Global Warming on Severe Thunderstorms in the United States. *Journal of Climate, 28*(6), 2443–2458. https://doi.org/10.1175/JCLI-D-14-00382.1.

Skamarock, W., Klemp, J., Dudhia, J., Gill, D., Barker, D., Wang, W., et al. (2008). *A Description of the Advanced Research WRF Version 3* [Application/pdf] (p. 1002 KB). UCAR/NCAR. https://doi.org/10.5065/D68S4MVH.

Smith, W. (2020). The cost of stratospheric aerosol injection through 2100. *Environmental Research Letters, 15*(11), 114004. https://doi.org/10.1088/1748-9326/aba7e7.

Sobash, R. A., Romine, G. S., Schwartz, C. S., Gagne, D. J., & Weisman, M. L. (2016). Explicit Forecasts of Low-Level Rotation from Convection-Allowing Models for Next-Day Tornado Prediction. *Weather and Forecasting, 31*(5), 1591–1614. https://doi.org/10.1175/WAF-D-16-0073.1.

Steiner, M., Houze, R. A., & Yuter, S. E. (1995). Climatological Characterization of Three-Dimensional Storm Structure from Operational Radar and Rain Gauge Data. *Journal of Applied Meteorology and Climatology, 34*(9), 1978–2007. https://doi.org/10.1175/1520-0450(1995)034<1978:CCOTDS>2.0.CO;2.

Sun, L., Hurrell, J.W., Rasmussen, K.L., Summers, B., Sherman, L., Kravitz, B. (2025). Assessing the Impact of Solar Climate Intervention on Future U.S. Weather Using a Convection-Permitting Model. (Manuscript in preparation).

The Royal Society. (2009). *Geoengineering the climate: science, governance and uncertainty*. The Royal Society. Retrieved from https://royalsociety.org/news-resources/publications/2009/geoengineering-climate/.

Thompson, G., Field, P. R., Rasmussen, R. M., & Hall, W. D. (2008). Explicit Forecasts of Winter Precipitation Using an Improved Bulk Microphysics Scheme. Part II: Implementation of a New Snow Parameterization. *Monthly Weather Review, 136*(12), 5095–5115. https://doi.org/10.1175/2008MWR2387.1.

Tian, B., Held, I. M., Lau, N.-C., & Soden, B. J. (2005). Diurnal cycle of summertime deep convection over North America: A satellite perspective. *Journal of Geophysical Research: Atmospheres, 110*(D8). https://doi.org/10.1029/2004JD005275

Tilmes, S., Richter, J. H., Kravitz, B., MacMartin, D. G., Mills, M. J., Simpson, I. R., et al. (2018). CESM1(WACCM) Stratospheric Aerosol Geoengineering Large Ensemble Project. *Bulletin of*

the American Meteorological Society, 99(11), 2361–2371. https://doi.org/10.1175/BAMS-D-17-0267.1.

Timmreck, C. (2012). Modeling the climatic effects of large explosive volcanic eruptions. *WIREs Climate Change, 3*(6), 545–564. https://doi.org/10.1002/wcc.192.

Touma, D., Hurrell, J. W., Tye, M. R., & Dagon, K. (2023). The Impact of Stratospheric Aerosol Injection on Extreme Fire Weather Risk. *Earth's Future, 11*(6), e2023EF003626. https://doi.org/10.1029/2023EF003626.

Trapp, R. J., & Hoogewind, K. A. (2016). The Realization of Extreme Tornadic Storm Events under Future Anthropogenic Climate Change. *Journal of Climate, 29*(14), 5251–5265. https://doi.org/10.1175/JCLI-D-15-0623.1.

Trapp, R. J., Diffenbaugh, N. S., Brooks, H. E., Baldwin, M. E., Robinson, E. D., & Pal, J. S. (2007). Changes in severe thunderstorm environment frequency during the 21st century caused by anthropogenically enhanced global radiative forcing. *Proceedings of the National Academy of Sciences, 104*(50), 19719–19723. https://doi.org/10.1073/pnas.0705494104.

Trapp, R. J., Hoogewind, K. A., & Lasher-Trapp, S. (2019). Future Changes in Hail Occurrence in the United States Determined through Convection-Permitting Dynamical Downscaling. *Journal of Climate, 32*(17), 5493–5509. https://doi.org/10.1175/JCLI-D-18-0740.1.

Trapp, R. J., Woods, M. J., Lasher-Trapp, S. G., & Grover, M. A. (2021). Alternative Implementations of the "Pseudo-Global-Warming" Methodology for Event-Based Simulations. *Journal of Geophysical Research: Atmospheres, 126*(24), e2021JD035017. https://doi.org/10.1029/2021JD035017.

van Vuuren, D. P., Edmonds, J., Kainuma, M., Riahi, K., Thomson, A., Hibbard, K., et al. (2011). The representative concentration pathways: an overview. *Climatic Change, 109*(1), 5. https://doi.org/10.1007/s10584-011-0148-z.

World Economic Forum. (2025). The Global Risks Report 2025. Clogny/Geneva, Switzerland. Retrieved from https://www.weforum.org/publications/global-risks-report-2025/in-full/.

Zarnetske, P. L., Gurevitch, J., Franklin, J., Groffman, P. M., Harrison, C. S., Hellmann, J. J., et al. (2021). Potential ecological impacts of climate intervention by reflecting sunlight to cool Earth. *Proceedings of the National Academy of Sciences, 118*(15), e1921854118. https://doi.org/10.1073/pnas.1921854118.

Zipser, E. J., Cecil, D. J., Liu, C., Nesbitt, S. W., & Yorty, D. P. (2006). WHERE ARE THE MOST INTENSE THUNDERSTORMS ON EARTH? *Bulletin of the American Meteorological Society, 87*(8), 1057–1072. https://doi.org/10.1175/BAMS-87-8-1057.